J. Fluid Mech. (2004), *vol.* 515, *pp.* 261–292.
DOI: 10.1017/S0022112004000461 Printed in the United Kingdom

Shear flow of a suspension of bubbles rising in an inclined channel

By ROBERTO ZENIT[1], YING H. TSANG[2], DONALD L. KOCH[2] AND ASHOK S. SANGANI[3]

[1]Instituto de Investigaciones en Materiales, Universidad Nacional Autónoma de México, México D.F. 04510, México

[2]School of Chemical Engineering, Cornell University, Ithaca NY 14853, USA

[3]Department of Chemical Engineering and Materials Science, Syracuse University, Syracuse NY 13244, USA

(Received 5 August 2002 and in revised form 5 May 2004)

A weak, laminar shear flow of a monodisperse suspension of high-Reynolds-number, low-Weber-number bubbles is studied in a novel experimental configuration. Nitrogen bubbles are formed through an array of small capillaries at the base of a tall channel with a small inclination from the vertical. The bubbles generate a unidirectional shear flow, in which the denser suspension near the bottom wall falls and the lighter suspension near the top wall rises. Profiles of the bubble and liquid velocities and the bubble volume fraction are obtained using hot-film and dual impedance probes. To our knowledge, measurements of the laminar shear properties of a nearly homogeneous bubble suspension have not previously been reported.

A steady shear flow is observed in which the bubble velocity variation across the channel is typically less than 20% of the mean bubble velocity. The velocity and volume fraction gradients increase with channel inclination and exhibit little or no dependence on the mean gas volume fraction. To explain the magnitude of the volume fraction gradients, it is necessary to consider the effects of both the lift force and the effective bubble-phase diffusivity in balancing the segregating tendency of the cross-channel component of the buoyancy force. The bubble velocity gradient can be understood in terms of a balance of the component of the buoyancy force parallel to the channel walls and an effective viscosity associated with the Reynolds stresses produced by bubble-induced liquid velocity fluctuations. Theories for bubbles rising with potential-flow hydrodynamic interactions predict an instability of the homogeneous state due to a negative Maxwell pressure. However, the hydrodynamic diffusivity inferred from our experiments is large enough to mitigate the clustering effects of the Maxwell pressure. Consistent with this, a vigorous instability of the homogeneous state of the bubble suspension is only observed at volume fractions larger than 5%–20% with the critical volume fraction depending on the angle of inclination.

1. Introduction

To understand the flow behaviour of suspensions and multiphase systems, it is useful to first study relatively simple flows of nearly homogeneous suspensions, for example, the sedimentation or rise of particles, drops or bubbles due to buoyancy in an otherwise quiescent fluid or the simple shear flow of a homogeneous suspension. It is also simplest to understand nearly monodisperse bubble or drop suspensions

in which no significant amount of coalescence is occurring. While studies of the effective viscosity and effective particle diffusivity in suspensions of solid particles in very viscous fluids are common (Leighton & Acrivos 1987), comparable experimental studies are lacking for flows in which the inertia of the continuous phase plays an important role in the particle length scale. One type of inertial suspension that has been the subject of considerable theoretical investigation is a suspension of high-Reynolds-number, low-Weber-number bubbles. The Reynolds number is defined as $Re = \rho_f d_b u_b/\mu$, where ρ_f is the fluid density, d_b is the bubble diameter, u_b is the bubble velocity relative to the fluid and μ is the fluid viscosity. The Weber number is defined as $We = \rho u_b^2 d_b/\sigma$, where σ is the surface tension of the liquid–gas interface. In this paper, we present an experimental investigation of the shear flow of a nearly homogeneous, monodisperse suspension of bubbles with high Reynolds number and moderately small Weber number.

The fluid velocity disturbances produced by high-Reynolds-number, low-Weber-number bubbles are expected to be well-approximated as potential flow fields. The experimental system that best approximates this limit is gas bubbles in water with diameters d_b from 0.5 to 1.5 mm corresponding to Re from 10 to 10^2 and to We from 10^{-3} to 10^{-1}. Some experimental confirmation of this expectation is obtained by comparing the rise velocity of bubbles with a calculation based on the viscous dissipation occurring in a nearly inviscid potential flow (Duineveld 1995). Detailed equations of motion can be derived from first principles for bubbles with potential-flow velocity disturbances (Biesheuvel & Gorissen 1990; Sangani & Didwania 1993*a*; Zhang & Prosperetti 1994; Bulthuis, Prosperetti & Sangani 1995; Yurkovetsky & Brady 1996; Kang *et al.* 1997; Spelt & Sangani 1998). Numerical simulations of many interacting spherical bubbles have also been performed (Smereka 1993; Sangani & Didwania 1993*b*). Of particular interest for our study are the theoretical and simulation studies of Kang *et al.* (1997) for simple shear flow of a bubble suspension in the absence of buoyancy forces and the study of Spelt & Sangani (1998) that derives equations of motion for a bubble suspension with a mean relative velocity of the two phases and a bubble velocity variance.

Theories and numerical simulations of bubbles with potential-flow interactions indicate that bubbles rising in a fluid tend to cluster so that a homogeneous suspension is unstable (Sangani & Didwania 1993*b*; Smereka 1993). In Zenit, Koch & Sangani (2001), we performed experiments on the rise of bubbles of approximately 1.4 mm diameter through a quiescent aqueous electrolyte solution. The bubbles were released from a uniform array of capillaries at the based of a tall thin vertical channel. The Reynolds number of the bubbles was very large ($380 > Re > 250$). The Weber number was moderately small ($1.5 > We > 0.5$). The individual bubbles rising in the liquid took on a spheroidal shape and had a rise velocity that could be explained by potential-flow theory for a deformed bubble. With increasing bubble concentration, the bubbles were found to become more spherical. The decrease in the mean rise velocity of the bubbles $\langle u_b \rangle$ with increasing bubble concentration was comparable with that predicted theoretically by Spelt & Sangani (1998).

Visual evidence of the clustering predicted by potential-flow theories was also obtained by Zenit *et al.* (2001), but the intensity of the clustering was considerably less than that observed in numerical simulations such as those of Sangani & Didwania (1993*b*). The fluid velocity variance was much larger than that predicted based on the potential-flow velocity disturbance of a homogeneous bubble suspension. The frequency spectrum of the Eulerian velocity indicated that most of the energy of the flow was contained at frequencies $\langle u_b \rangle / W$ associated with the passage of clusters of

bubbles with a size comparable with the gap thickness W of the channel. The frequency spectrum did not exhibit the ω^{-2} scaling that would be expected of a single-phase turbulent flow. Nonetheless the large velocity fluctuations produced by the instability of the bubble suspension may be expected to significantly influence the transport (or dispersion) of bubbles and the transport of momentum in vertical and slightly inclined channels. Large velocity fluctuations have also been measured in high-Reynolds-number suspensions of rising bubbles in water with diameters of about 5 mm (Lance & Bataille 1991) and falling solid particles in water (Parthasarathy & Faeth 1990). These authors attributed the liquid velocity fluctuations to the disturbances in the wakes of the bubbles or particles. The 1.4 mm bubbles studied in Zenit *et al.* (2001) and the present study are expected to have much weaker wakes and we attribute the large velocity fluctuations to the clustering of the bubbles.

In the present paper, we will investigate the shear flow of a bubble suspension. In previous investigations involving sheared bubbly liquids, the shear flow was induced by a pressure gradient along the axis of a pipe (Wang *et al.* 1987; Liu & Bankoff 1993*a*, *b*). In the resulting strong shear flows, the bubble volume fraction is usually highly inhomogeneous, i.e. the ratio of the volume fraction to the magnitude of the bubble volume fraction gradient is comparable with the bubble diameter in parts of the flow. Also, most of these investigations involve very high-speed flows that are probably turbulent and large deformed bubbles whose disturbances to the fluid velocity would not be expected to be described by potential flow. Valukina's, Koz'menko & Kashinskii (1979) study of vertical pressure-driven pipe flow of bubbles in an electrolyte solution does conform to the high-Reynolds-number, low-Weber-number limit. However, the range of conditions investigated and the characterization of the flows were limited and some of the experiments involved situations in which all the bubbles were confined to a layer about 1.5 bubble diameters thick near the pipe wall.

We use a novel method to produce a weakly sheared, nearly homogeneous bubble suspension. In particular, we incline the channel used in our previous investigation at small angles (up to 10°) from the vertical. This leads to a steady, buoyancy-driven shearing flow in which the more buoyant suspension near the top wall translates upward and the suspension near the bottom wall translates downward. The shear flow thus produced is a weak perturbation to the mean rise of the bubbles through the liquid. The variation in the bubble velocity across the channel width is less than about 20% of the mean rise velocity. The Reynolds number associated with the mean velocity of the liquid and the gap thickness of the channel is less than 1000 so that (based on single-phase flow criteria) the flow is expected to be laminar. Buoyancy-driven flows due to small mis-alignments are known to be important in bubble columns (Lu *et al.* 1997) and fluidized beds (Couderc 1985). In addition, the segregation and buoyancy-driven flows have a strong influence on oil and natural gas wells, which typically involve two or three phases (oil, gas and water) and are drilled at an angle to the vertical. However, we believe this is the first attempt to use an inclined channel to produce a nearly viscometric flow.

In low-Reynolds-number suspensions, a pure shear flow with no relative motion of the two phases can be achieved by using a very viscous fluid or by matching the density of the particles or drops with that of the fluid. At higher Reynolds numbers, density matching is also possible though we are not aware of an ideal viscometric study of a high-Reynolds-number sheared particle suspension. In any case, density matching is impossible for bubble suspensions and so one must always consider a mixed buoyancy–shear flow for terrestrial experiments involving bubbly liquids.

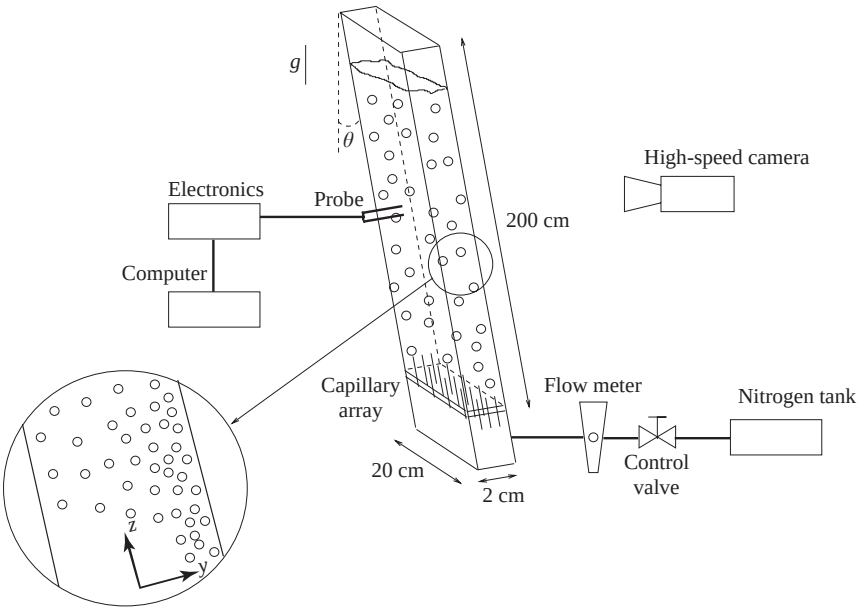

FIGURE 1. Experimental setup. The insert shows schematically the accumulation of bubbles near the top of the channel.

We believe that the present study is the most ideal example of a sheared bubbly liquid investigated to date.

The experimental setup and experimental measurements are described in §§ 2 and 3, respectively. Many of the measurement techniques are similar to those used in our previous study of bubble suspensions in a vertical channel (Zenit *et al.* 2001). Measurements of the profiles of bubble velocity, bubble velocity variance and bubble concentration were obtained using a dual impedance probe. Details of the experimental technique using the dual impedance probe can be found in Zenit, Koch & Sangani (2003). In § 4, these measurements are discussed and interpreted.

2. Experimental setup

We study the shear flow of a bubble suspension in the inclined channel shown schematically in figure 1. Nitrogen bubbles are injected through a capillary array at the base of a tall narrow channel which is inclined at a small angle θ with respect to the vertical. The channel is 20 cm wide with a 2 cm gap and 150 cm high filled with a dilute aqueous electrolyte solution (0.05 mol l^{-1} $MgSO_4$) to inhibit bubble–bubble coalescence. The streamwise (parallel to the walls) and cross-streamwise (perpendicular to the walls) directions, will be referred to as the z- and y-directions respectively. W is the channel thickness.

The mean gas volume fraction, α, or hold up, is obtained from the increase ΔH in liquid level after the bubbles are introduced to the cell,

$$\alpha = (H_o/\Delta H + 1)^{-1} \tag{2.1}$$

where H_o is the initial liquid level. Although there are concentration gradients within the channel, the hold up gives us a measure of the average gas volume fraction. The bubble size and shape are determined using high-speed video photographs and digital image processing.

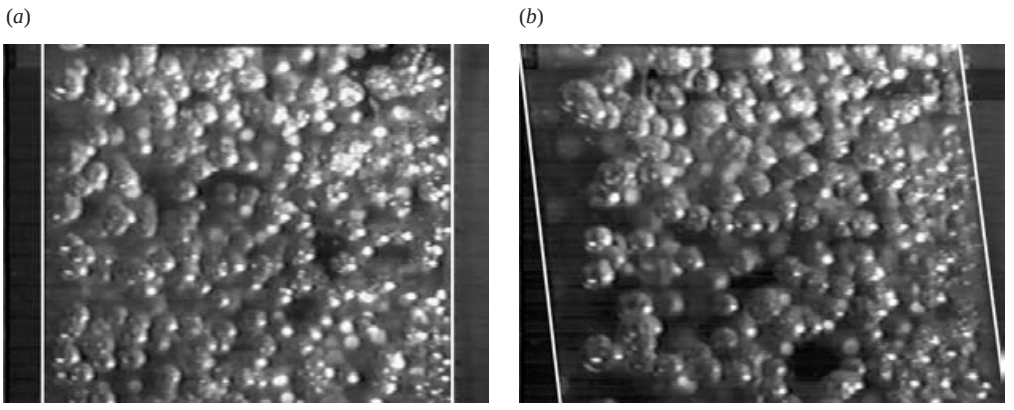

FIGURE 2. Photo of the flow taken from the sidewall. (*a*) Vertical channel, $\theta = 0°$, (*b*) inclined channel, $\theta = 5°$. Mean gas volume fraction, $\alpha = 0.05$. The slight increase in concentration near the top wall can be appreciated.

Due to the inclination of the channel a small component of the gravity vector acts in the gap thickness direction. As a result the bubbles tend to accumulate at the top part of the gap. The suspension near the top of the channel has a lower mass density and therefore rises. A velocity gradient is generated and the suspension is sheared. Figure 2 shows photographs of suspensions in vertical and inclined channels with the same average bubble concentration ($\alpha \approx 0.05$). The fluctuating motion of the bubbles and frequent bubble–bubble collisions as well as the mean shearing of the bubble phase are apparent in a videotape of the suspension.

Measurements of the variation of the suspension properties across the gap were obtained using two types of probe. A commercial hot-wire probe detected the liquid velocity. A dual impedance probe was used to measure the bubble concentration, and the mean and variance of the bubble velocity.

It is important to note that the measurement of the gas volume fraction with the impedance probe was found to be sensitive to the bubble size and the details of the bubble–probe interaction. A detailed description of how to correct the impedance probe measurement to account for the bubble–probe interaction, as well as a complete description of the measuring system, can be found in Zenit *et al.* (2003). A translating device to which the probes were attached was fixed to one of the walls. The position could be resolved to within 0.1 mm and measurements were taken at 25 positions across the 2 cm gap for all experiments to obtain an accurate account of the profiles. Measurements near the walls could not be obtained with a good degree of accuracy due to the probe–wall interaction.

The voltage signals obtained from the probes were digitized using a computer based data acquisition system with a sampling rate of 10 kHz for each probe. The recording time per data point was at least 100 s. The initial liquid height, H_o, was 1.50 m and was kept constant for all experiments.

2.1. *Gas volume fraction and bubble velocity measurement*

An impedance probe is used to measure the gas volume fraction, and the mean and variance of the bubble velocity. The system detects local changes in electrical impedance. It uses the difference in electrical impedance between the gas and liquid phases to determine the residence time of bubbles in a small measuring volume adjacent to the probe tip. The probe was designed such that it is able to identify single bubbles

in a small localized measuring volume. This characteristic is essential to measure the spatial variation of the bubble concentration and velocity across the thin direction of the channel. Making the measuring volume small has the disadvantage that the measurement becomes sensitive to the nature of bubble–probe interactions, especially for the determination of the gas concentration. Details of the probe operation, construction and performance assessment can be found in Zenit *et al.* (2003).

To measure the bubble velocity a second probe, of identical characteristics, is placed a short distance downstream of the leading probe. The signals of the two probes are cross-correlated to find the time delay between them. The time delay is the time that a bubble takes to move from the leading to the trailing probe; hence, by knowing the distance between the two probe tips, the velocity can be calculated. The mean bubble velocity is obtained from the cross-correlation of long duration traces during which many bubbles pass near the two probes. By identifying individual bubble events within the probes signals, a distribution of bubble velocities can be obtained and, therefore, the bubble velocity variance can also be calculated. For the measurements presented in this paper the probe is inclined along with the channel; hence, the velocity measured is in fact the component parallel to the walls.

2.2. *Liquid velocity and wall shear stress measurements*

A hot-film anemometer is used to measure the liquid velocity in the bubble suspension. For the case of gravity-driven bubbly flows the mean liquid velocities are small and the distinction between the measured mean and fluctuating components is very difficult to assess. The main complication in the interpretation of the velocity signal arises from the fact that the probe can only measure the absolute value of the fluid velocity. Usually hot-film probes are used in flows with a large mean velocity and small fluctuating velocity and then one can easily discern the statistics of the velocity fluctuations relative to the mean. However, in the inclined channel, the mean liquid velocity is expected to be only about 0.1 times the root-mean-square of the liquid velocity fluctuations. Nonetheless, we can unambiguously present measurements of the mean-square velocity. This contains contributions due to the mean velocity associated with the shearing of the suspension as well as the liquid velocity fluctuations produced by the bubbles, although we expect the latter to dominate. Details of the performance of the hot-wire anemometer can be found in Zenit *et al.* (2001).

A second hot-film probe was used to measure the wall shear stress. The probe consisted of a heating element located at its tip, which is connected to the hot-wire anemometry system. The heating patch, with a dimension of 0.15 mm by 1.5 mm, is made of platinum with a layer of quartz coated on top which is necessary to protect the sensor from shorting in the conducting salt solution. The probe was flush mounted to the channel wall and oriented in such a way that the longer side of the heating patch is normal to the main flow direction. By measuring the electric voltage needed to maintain the probe at a constant temperature, the rate of heat transfer can be inferred. Since the thermal boundary layer is thinner than the momentum boundary layer, this heat transfer rate is proportional to the velocity gradient at the wall and the shear stress. The probe was calibrated by imposing the known laminar flow associated with a developing boundary layer on a flat plate for a range of free-stream velocities and angles of inclination of the plate to the free-stream velocity. In addition to calibrating the probe, the consistency of the measurements obtained for different angles of inclination validated the ability of the probe to detect the local shear stress. More information about the performance of this type of wall shear probe can be found in Jensen, Sumer & Fredsoe (1989).

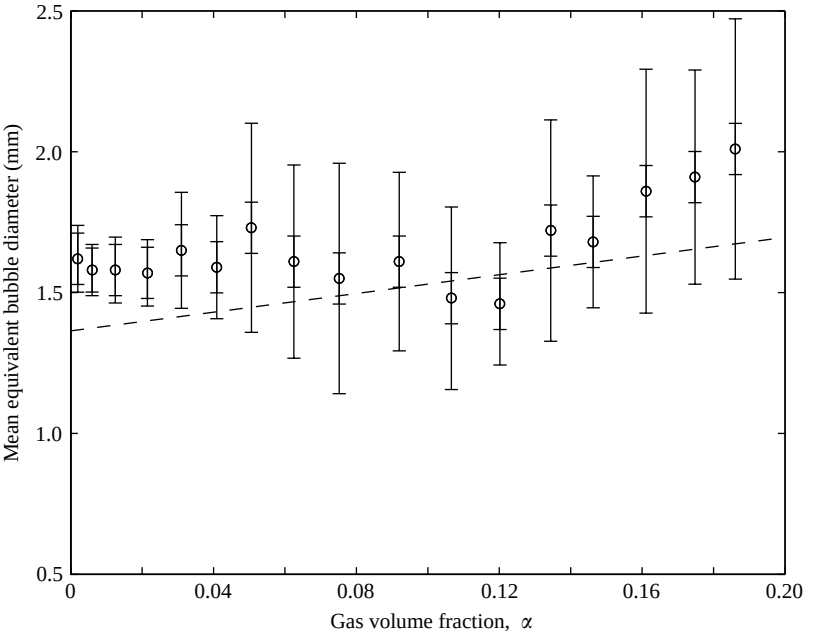

FIGURE 3. Equivalent bubble diameter, d_{eq}, as a function of mean gas volume fraction, α, for a channel inclination of $\theta = 5^\circ$. The short bars indicate the measurement error associated with the finite pixel size. The long bars indicate the bubble size standard deviation. The dashed line shows the equivalent bubble size best-fit from the experiments in a vertical channel (Zenit *et al.* 2001).

3. Experiments

Profiles of the concentration, bubble velocity and liquid velocity were obtained for three mean volume fractions ($\alpha = 0.02$, 0.05 and 0.10) at five channel inclinations ($\theta = 0^\circ$, 2.5°, 5°, 7.5° and 10°). The measurements were taken at 20 positions across the gap with a 1 mm increment. Measurements near the walls were discarded since it was not possible to discriminate between the effects of the wall–probe and the bubble–wall interactions.

To verify that the flow was fully developed a series of measurements were also obtained for three different axial positions. Some single bubble experiments were also performed to observe the motion of a bubble interacting with the inclined walls.

3.1. *Bubble size*

The effect of the inclination of the channel on the bubble size was determined using a procedure for assessing bubble size similar to that used in Zenit *et al.* (2001). Photographs of the flow were digitized and processed for different values of the mean bubble concentration. We present results for a channel with an inclination $\theta = 5^\circ$.

The bubble equivalent diameter was obtained from the two-dimensional photographic projection of the spheroidal bubbles and calculated as

$$d_{eq} = \left(d_{long}^2 d_{short}\right)^{1/3}. \tag{3.1}$$

Figure 3 shows the measured bubble equivalent diameter as a function of the mean gas volume fraction. It is observed that the bubble size stays approximately constant for volume fractions below 0.14. The measured bubble size is 9% larger than that found in the vertical channel experiments (Zenit *et al.* 2001).

The statistical error associated with the size measurement is on the order of 3%. We used a constant value of the bubble diameter to calculate the correction for the gas volume fraction caused by bubble–probe excluded volume. Since measurements of the bubble size were obtained only for a channel inclination of 5° and the effects of inclination and the associated shear flow on the bubble size are modest, it is assumed that the results for 5° can be applied to all inclinations. The aspect ratio of the bubbles, $\chi = d_{long}/d_{short}$, was also measured from the photographs. It was found to be approximately constant, $\chi = 1.15 \pm 0.05$, for gas volume fraction up to 0.10 for all the channel inclinations tested.

3.2. *Axial flow development*

To confirm that the experiments were taken far enough above the channel bottom to correspond to a fully developed state, velocity and bubble volume fraction profiles were obtained at three axial positions, cf. figure 4(a, b). These profiles were obtained by inserting the probe from the top wall, which corresponds to the position $y = 10$ mm on the graphs, and translating it to different positions within the gap.

The results clearly show that the flow is already developed at a position of 78.3 cm above the bottom of the channel. As discussed in Zenit *et al.* (2003), some increase of the gas volume fraction can be expected resulting from the volumetric expansion due to the loss of hydrostatic head (less than 4% for the present conditions). This effect can be observed in the measurement obtained at an axial position of 138 mm. All the gas volume fraction measurements were corrected for the probe–bubble interaction mechanism described in Zenit *et al.* (2003). In figure 4, the measurements near the walls are shown.

The measured volume fraction is nearly uniform at the centre of the channel and appears to decrease near the wall through which the probe is being inserted. This decrease arises because the wall excludes bubbles from entering a portion of the measuring volume near the tip of the probe. For measurements near to the opposite wall, the gas volume fraction appears to increase. This increase is most likely a result of the probe intrusion. Bubbles were observed to be 'trapped' or retarded in the gap between the tip of the probe and the wall. Note that, with the present probe setup, the shape of the the bubble volume fraction profile can be determined accurately only in the region away from the wall. It is not possible to determine to what extent the decrease of the gas volume fraction and bubble velocity is caused by the intrusive nature of the probe. To avoid this uncertainty, the data are reported only for regions 'far' from the walls. In the subsequent figures of this paper, the measurements are shown for distances of approximately two bubble diameters away from each wall.

3.3. *Gas volume fraction profiles*

The measured gas volume fraction profiles for the experimental set are shown in figure 5. From these results, the concentration gradient can be calculated. A value of the gas volume fraction gradient ($\partial\alpha/\partial y$) is calculated and made non-dimensional as

$$\widehat{\frac{\partial \alpha}{\partial y}} = d_b \frac{\partial \alpha}{\partial y}, \tag{3.2}$$

where $\partial\alpha/\partial y$ is calculated by fitting the measurements to a straight line. This expression assumes that the profile is linear. From figure 5 it can be seen that this assumption is valid. The data for measurements within three bubble diameters of either wall were discarded to calculate the gradient.

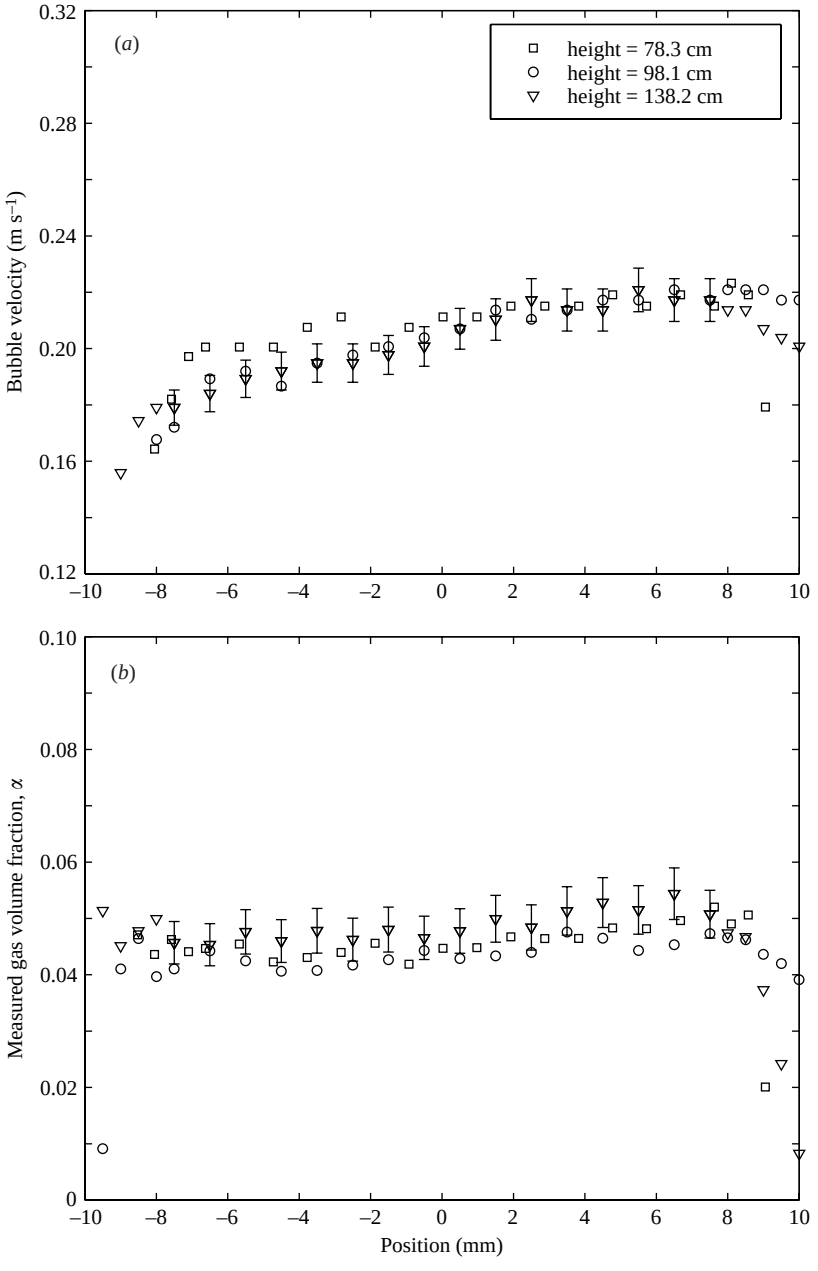

FIGURE 4. (*a*) Bubble velocity and (*b*) gas concentration profiles for three axial positions. Channel inclination $\theta = 5°$. Mean gas volume fraction $\alpha = 0.05$. The centre of the channel corresponds to position = 0. The error bars show the typical experimental uncertainties of the measurements.

Figure 6 shows the gradient of the bubble concentration as a function of the channel inclination for the three mean gas volume fractions tested. Within the experimental error the trend is clear. The gradient of bubble concentration increases linearly with channel inclination and is not affected significantly by the mean gas volume fraction

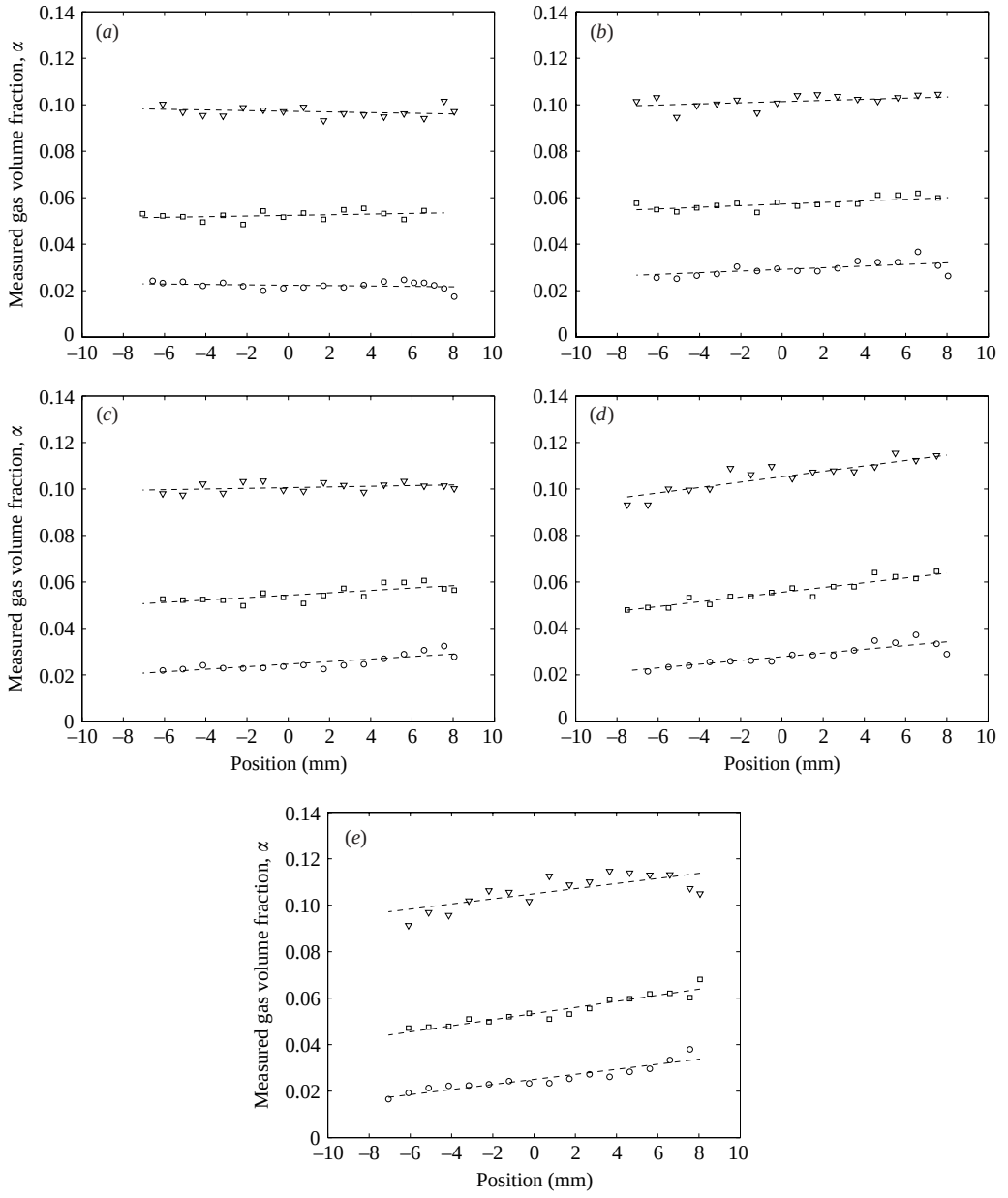

FIGURE 5. Gas volume fraction profiles for three typical hold ups. ○, $\alpha = 0.02$; □, $\alpha = 0.05$; ▽, $\alpha = 0.10$, for a vertical channel and four channel inclinations: (*a*) $\theta = 0°$, (*b*) 2.5°, (*c*) 5°, (*d*) 7.5°, (*e*) 10°. The lines show linear fits to the data excluding the near-wall regions.

of the channel. The solid line shown on the figure corresponds to the linear fit

$$\widehat{\frac{\partial \alpha}{\partial y}} = \kappa_0 \theta \tag{3.3}$$

where $\kappa_0 = 2.147 \times 10^{-4}$ and θ is expressed in degrees.

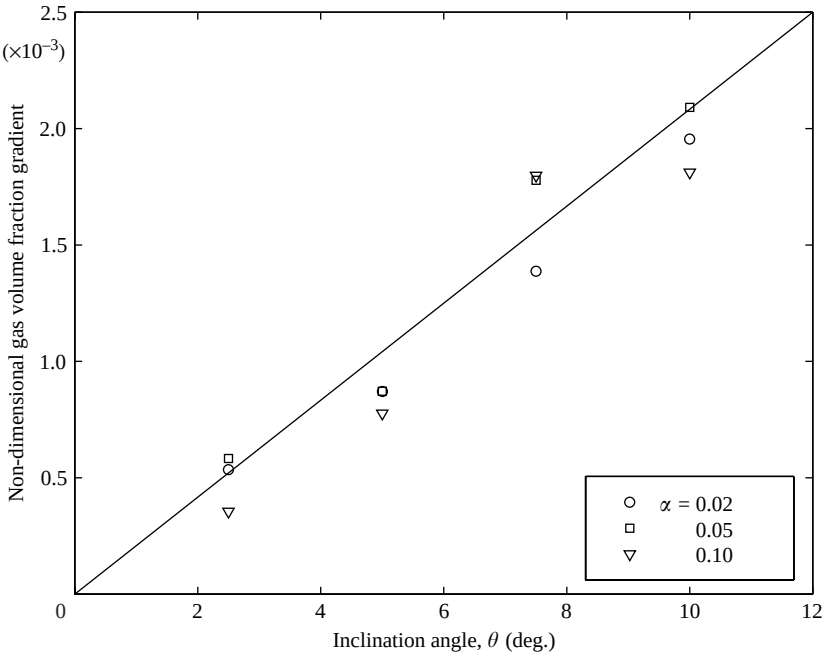

FIGURE 6. Non-dimensional gas volume fraction gradient as a function of channel inclination angle for three different gas volume fractions. The solid line shows the best fit equation (3.3).

3.4. *Bubble velocity profiles*

The profiles of the mean bubble velocity are presented in figure 7. The bubble velocity is constant throughout most of the vertical channel. In the inclined channels the bubbles in the high-volume-fraction region near the upper wall ($y = 10$ mm) rise faster than those in the low-volume-fraction region near the lower wall ($y = -10$ mm). The bubble velocity increases monotonically with increasing y in the centre of the gap. We observed a decrease of the bubble velocity near the walls. However, it is not reported here since it is not possible to discriminate between the effect caused by the intrusive nature of the probe and the bubble–wall interaction mechanisms.

As the concentration and the inclination of the channel increase, the bubble velocity measurements become more scattered. In fact, the measurements for $\alpha = 0.10$ at an inclination of $\theta = 10^\circ$ are not shown, as for this case the flow became very agitated; hence, it was not possible to obtain accurate results. The increased scatter can already be observed for the $\alpha = 0.05$ and $\theta = 10^\circ$ case. As we will discuss later, the flow within the channel becomes unsteady at larger values of α and θ. The instability manifests itself as macroscopic vortical structures that move across the width and length of the channel. This instability is much more vigorous and visually apparent than the mild clustering of bubbles at small α and θ discussed in the introduction and in Zenit *et al.* (2001). The large unsteady motions of the suspension make the measurement of bubble velocity profiles more inaccurate in two ways. First, the motion of the bubbles is no longer quasi-uni-directional. The horizontal component of the velocity disturbance produced by the instability could cause bubbles detected by the leading probe of the dual impedance probe to be swept away before encountering the trailing probe so that no velocity measurement can be obtained: Indeed, we found that 12% of the bubble probe encounters at $\theta = 10^\circ$ failed to produce a velocity

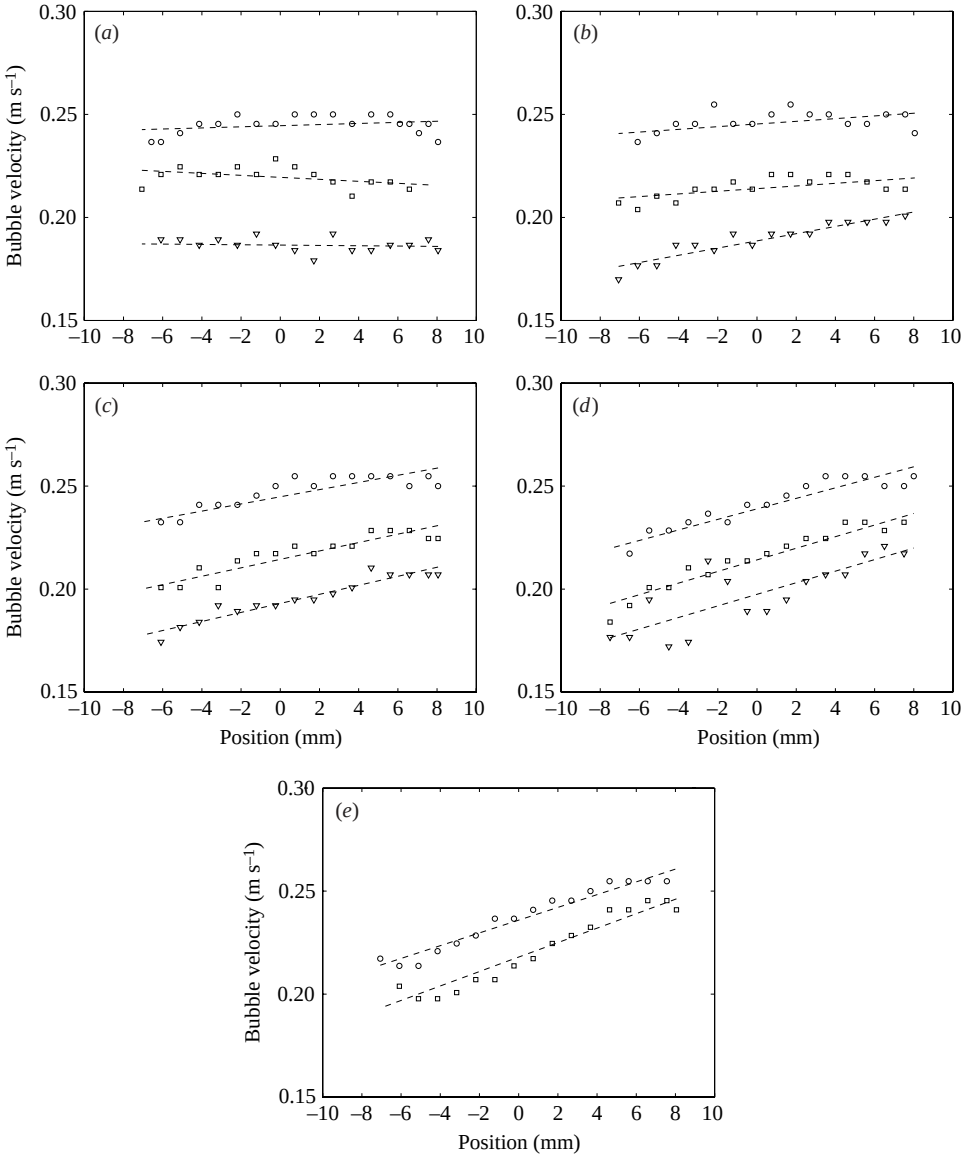

FIGURE 7. Bubble velocity profiles for three typical hold ups. ○, $\alpha = 0.02$; □, $\alpha = 0.05$; ▽, $\alpha = 0.10$, for a vertical channel and four channel inclinations: (*a*) $\theta = 0°$, (*b*) 2.5°, (*c*) 5°, (*d*) 7.5°, (*e*) 10°. The lines show the linear best fits.

measurement for this reason, compared with 8% in the vertical channel case. Perhaps more importantly, the unsteady motions have a much longer correlation time than the velocity disturbances produced by bubbles in a more homogeneous suspension. Since the temporal averaging was conducted over a fixed time period of 100 s for all the conditions, we may then expect to have less statistical significance for the measurements taken in the unstable suspensions.

The bubble velocity gradient was obtained by fitting the measurements to a straight line. As the inclination of the channel increases the bubble velocity gradient increases. The gradient of the bubble velocity appears to be weakly dependent on the mean

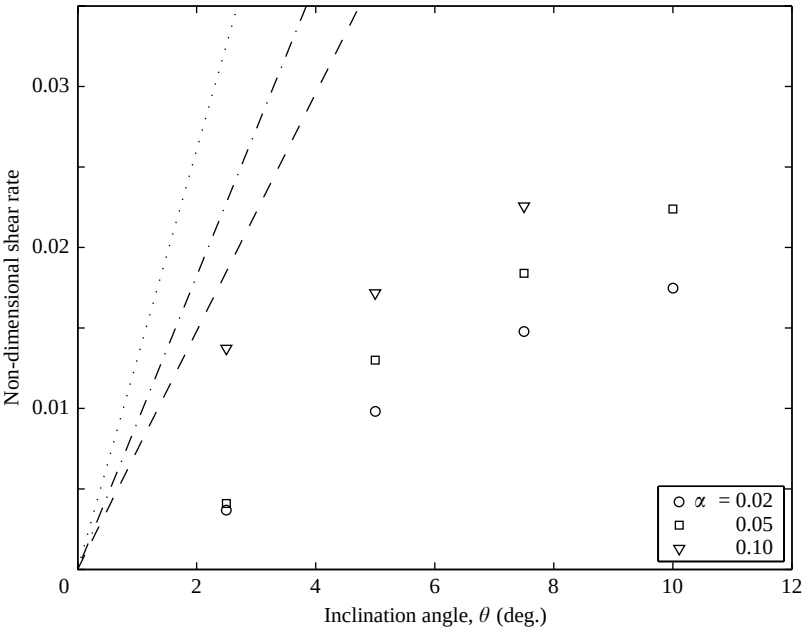

FIGURE 8. Non-dimensional bubble velocity gradient as a function of channel inclination angle for three different gas volume fractions. The solid line shows the best linear fit. The lines show predictions from (4.2) for $\alpha = 0.02$ (– – –); $\alpha = 0.05$ (– · –) and $\alpha = 0.10$ (· · ·).

gas volume fraction. Figure 8 shows the non-dimensional bubble velocity gradient, $\partial \widehat{u_b/\partial y}$, calculated using

$$\widehat{\frac{\partial u_b}{\partial y}} = \frac{(\partial u_b/\partial y)d_b}{\langle v_b \rangle} \tag{3.4}$$

where $\partial u_b/\partial y$ is the measured change in bubble velocity for the reported data (that excludes the regions near the walls), which represent the slope of the linear fits shown in the figures. The bubble diameter of $d_b = 1.55$ mm is obtained from figure 3. We use the relative velocity of the bubble and the fluid averaged across the gap to non-dimensionalize the bubble velocity. The relative velocity v_b is assumed to be the same in the inclined channel as that occurring at the same volume fraction in a vertical channel so that $\langle v_b \rangle$ is calculated using equation (3.4) of Zenit *et al.* (2001). Because the angles of inclination are small and the relative velocity in a fully developed flow is expected to arise from a balance of buoyancy and drag forces, we believe this approximation is reasonable. Figure 8 shows clearly that the gradient increases linearly with the channel inclination and that it also increases with increasing mean gas volume fraction. The data can be fitted to

$$\widehat{\frac{\partial u_b}{\partial y}} = \kappa_1 \theta \sqrt{\alpha} \tag{3.5}$$

where $\kappa_1 = 1.006 \times 10^{-2}$ and θ is measured in degrees.

3.5. *Bubble velocity variance*

The impedance probe was used to measure the velocities of many different bubbles at each position across the gap. Thus, we are able to quantify the bubble velocity

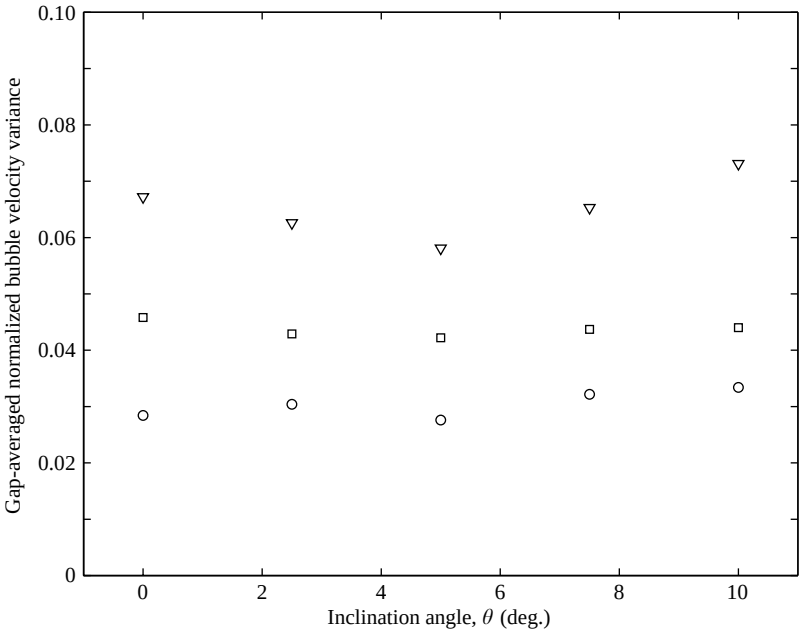

FIGURE 9. Gap-averaged normalized bubble velocity variance (z component) as a function of channel inclination for three typical hold ups. ○, $\alpha = 0.02$; □, $\alpha = 0.05$; ▽, $\alpha = 0.10$.

variance $\langle u_b'^2 \rangle$ or bubble-phase *temperature*. Typically, the bubble phase temperature is defined as $T = [\langle u_{bx}'^2 \rangle + \langle u_{by}'^2 \rangle + \langle u_{bz}'^2 \rangle]$. Here, since we are only able to measure the component of the variance of the bubble velocity in the z-direction, we define $T \approx \langle u_{bz}'^2 \rangle$.

The fluctuations in bubble velocity arise from shear-induced bubble–bubble collisions or from fluid velocity disturbances associated with the relative motion of the bubbles and liquid. Kang *et al.* (1997) argued that shear-induced collisions will produce a large velocity variance if the Reynolds number $Re_\gamma = a^2\gamma/\nu$ based on the bubble radius and the velocity gradient $\gamma = \partial u_b/\partial y$ is large. However, in our experiments Re_γ is always less than 1, so that shear-induced bubble velocity fluctuations are not expected to be very significant. In Zenit *et al.* (2001), we found that quite large bubble velocity variances can arise as bubbles rise in a vertical channel. It was thought that the magnitude of these fluctuations was enhanced by the formation of bubble clusters.

The velocity variance in the inclined channels was observed to vary slightly across the channel, being larger near the lower wall where the bubble volume fraction is smaller. If we assume that the mean relative velocity $\langle v_b \rangle$ of the bubble and liquid is only a function of the local volume fraction, as would be expected to occur if it arises purely from a balance of buoyancy and drag forces, then this average relative velocity is higher in the low-volume-fraction region. (Note that the pressure gradient in the liquid will be independent of y due to the unidirectional nature of the flow.) The normalized velocity variance $\langle u_b'^2 \rangle / \langle v_b \rangle^2$ was found to be nearly independent of position across the channel as might be expected if the velocity fluctuations arise from the relative motion of the phases. The normalized velocity variance averaged over the gap is plotted in figure 9. The normalized variance is nearly independent of the angle of inclination, suggesting that it arises purely from the relative motion

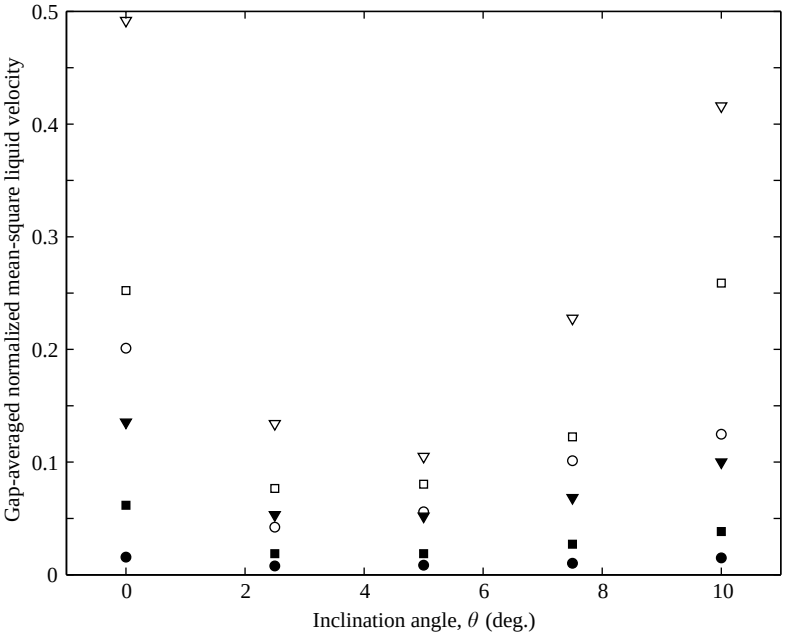

FIGURE 10. Gap-averaged mean-square liquid velocity as a function of channel inclination for three typical hold ups. ○, $\alpha = 0.02$; □, $\alpha = 0.05$; ▽, $\alpha = 0.10$. The empty and filled symbols show the measurements of the streamwise and crossstreamwise mean-square liquid velocity respectively.

and is independent of the shearing motion. The normalized variance increases with increasing bubble concentration.

3.6. *Mean-square liquid velocity*

The mean-square liquid velocity was measured at various positions across the channel using the hot-wire probe. By orienting the axis of the cylindrical heating element of the probe parallel and perpendicular to the walls, it was possible to determine the mean-square of the cross-streamwise and streamwise velocity components as described in Zenit *et al.* (2001). The mean-square liquid velocity normalized by the square of the mean relative velocity between the phases was nearly uniform across the channel cross-section. If we estimate the mean liquid velocity as comparable with the variation of the bubble mean velocity across the channel, then we conclude that the mean-square liquid velocity is dominated primarily by the variance of the velocity rather than by the square of the mean velocity. The mean-square liquid velocities averaged over the gap thickness are plotted in figure 10. The measurements are normalized by the gap-averaged mean bubble velocity, $\langle u_{lz}{}^2\rangle/\langle v_b\rangle^2$ and $\langle u_{ly}{}^2\rangle/\langle v_b\rangle^2$. For all concentrations and inclination angles, the mean-square horizontal velocity is about 20% of the mean-square vertical velocity. The mean-square liquid velocities are approximately proportional to the bubble volume fraction. It is interesting to note that the mean-square velocities have a non-monotonic dependence on the angle of inclination. Inclining the channel slightly from the vertical $\theta < 5^\circ$ leads to a decrease in the mean-square velocity. We might speculate that this slight inclination allows bubble clusters to stratify so that they produce a smaller disturbance. For angles above 5°, the variance increases with angle of inclination. This increase is especially pronounced for $\alpha = 0.1$ and $\theta = 10^\circ$, a condition for which we observed a vigorous

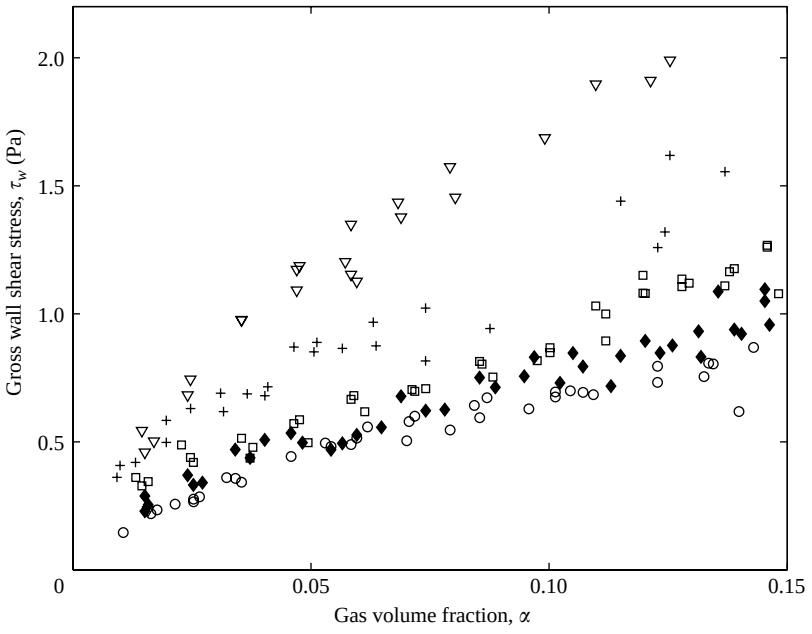

FIGURE 11. Gross wall shear stress τ_w as a function volume fraction α. Measurements at different angles: ○, vertical; ◆, 2.5°; □, 5°; +, 7.5°; ▽, 10°.

instability of the suspension with large vortical structures. Thus, we believe that the increase in the mean-square velocity for $\theta > 5°$ is a manifestation of this instability.

3.7. *Shear stress measurements*

Using a probe that works under the same principle as a hot-wire anemometer, a measurement of the absolute value of the shear stress was obtained. Ideally, to measure the liquid shear stress, we should only consider the signal arising from the probe when no bubble is directly in contact with the heating element. Observations of the collisions of single bubbles with the shear stress probe indicated that such collisions give rise to a large spurious signal and the bubble collisions have a greater influence on the shear stress measurement than on the measurement of liquid velocity in the middle of the channel by hot-wire probes. To minimize bubble–probe collisions, we will use measurements taken at the lower wall where the bubble concentration is smaller and where bubble–wall collisions are gentler due to the absence of a gravitational driving force for the collision. The absolute value of the shear stress was averaged over a period of 90 s for each volume fraction and inclination.

Figure 11 shows the measured shear stress. The measured shear stress increases with bubble volume fraction and inclination angle. The mean of the absolute value of the shear stress is non-zero even in a vertical channel, because bubbles passing the probe produce a fluctuating shear stress. This fluctuating shear stress increases with increasing volume fraction as the number of bubbles passing the probe grows. Since the boundary layer thickness on the channel wall due to the transient liquid flow caused by passage of a bubble scales with $aRe^{-1/2}$, the shear rate due to the passage of a bubble within a distance of about a bubble radius from the probe is $O(v_b/aRe^{1/2})$. Thus, the dimensionless shear rate is $O(Re^{-1/2}) = O(10^{-1})$. From figure 11, the results have the correct order of magnitude.

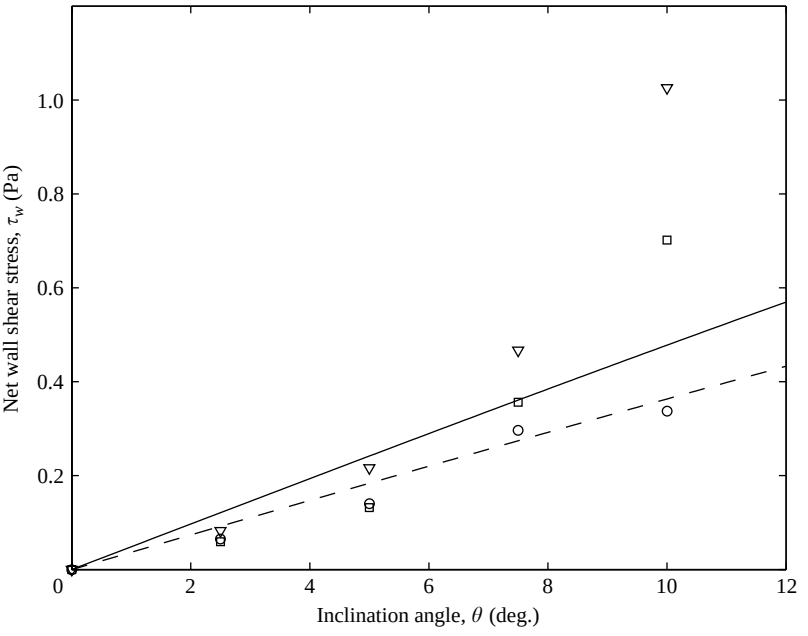

FIGURE 12. Net wall shear stress as a function of the channel inclination angle θ. Measurements at different gas volume fractions: ○, $\alpha = 0.02$; □, $\alpha = 0.05$; ▽, $\alpha = 0.10$. The lines represent the predictions from (4.14) for: —, $\lambda = 0$; – – –, $\lambda = 0.32$.

As the channel is inclined, a mean shear stress will develop in addition to the fluctuating shear stress produced by the discrete nature of the bubbles. We found that the standard deviation of the absolute value of the shear stress was nearly independent of θ for $\theta > 5^\circ$. This observation would be consistent with a scenario in which the fluctuations in the shear stress are independent of θ and the only effect of increasing θ is to increase the mean shear stress. Based on this observation, we will interpret the difference between the average absolute value of the shear stress in the inclined and vertical channel for the same α as the mean shear stress.

Clearly, the measured shear stress increases with gas volume fraction and channel inclination. The net shear stress obtained by subtracting the shear stress measurement from the corresponding stress measurement in a vertical channel is plotted as a function of inclination angle in figure 12 for three values of the bubble volume fraction.

4. Discussion and interpretation

The bubble volume fraction gradients measured in our experiments were surprisingly modest. In this section we will explore some of the possible mechanisms that may account for the order of magnitude of the bubble velocity and concentration gradients reported in this investigation.

4.1. *Lift forces*

We can try to explain the magnitude of the bubble velocity gradient using a simple model based on a force balance on the individual bubbles neglecting bubble–bubble interactions. Since the bubbles are exposed to a shear flow, a lift force will be exerted on them. In the simplest of cases, the sum of the lift force and the small component of

gravity in the direction of the channel gap $g \times \sin\theta$ will be zero. Assuming a simple form for the lift force on a spherical bubble in inviscid flow (Auton 1987):

$$F_L = -\frac{\pi}{6}\rho d_b^3 C_L v_b \frac{\partial u_l}{\partial y} \tag{4.1}$$

where v_b is the relative velocity of the bubble and the liquid, in the z-direction, $\partial u_l/\partial y$ is the liquid velocity gradient and $C_L = 0.5$ is the lift coefficient for inviscid shear flow with $\widehat{\partial u_b/\partial y} \ll 1$.

The liquid velocity gradient is assumed to be the same as the measured gradient of the bubble velocity because we have a fully developed uni-directional flow with a small variation of bubble volume fraction across the gap. In this situation, a substantial difference between the liquid and bubble velocity gradients could not be sustained over large distances (large compared with bubble radius). In pipe flow differences occur but only near the walls, within 2–3 bubble diameters from the wall (Liu & Bankoff 1993*a*, *b*). In this investigation we are only considering the measurements obtained away from the walls.

The bubble velocity relative to the liquid, in the z-direction, is estimated to be $u_b \cos\theta$, where u_b is the velocity obtained for bubbles of the same size in a vertical channel (cf. equation (3.4) of Zenit *et al.* 2001). Using these approximations and solving for the bubble velocity gradient yields

$$\frac{\partial u_b}{\partial y} = \frac{2g \tan\theta}{v_b}. \tag{4.2}$$

The lines in figure 8 show the predictions for the velocity gradient necessary to obtain a lift force that balances the cross-stream buoyancy force for three different gas volume fractions, i.e. three different mean bubble velocities. The experimentally measured bubble velocity gradients are plotted as symbols. The experiment and theory exhibit similar trends of increasing velocity gradient with increasing inclination and bubble volume fraction. However, the experimentally measured velocity gradients are about a factor of 2.5 smaller than the predictions based on the lift–buoyancy calculation. Thus, a lift coefficient of $C_L = 1.25$ would be required.

The lift coefficient $C_L = 0.5$ used to compute the curves in figure 8 is appropriate for spherical bubbles in the limits of infinite Reynolds number, zero bubble volume fraction, and small shear rates. To see if changes in C_L with Re, α, χ or shear rate could explain the discrepancy between the lift theory and the experiments, we will consider theoretical estimates for the magnitude of these effects. Numerical simulations of a clean spherical bubble in a simple shear flow (Magnaudet & Legendre 1998) indicate that at a Reynolds number $Re = 280$ typical of our experiments, the lift coefficient is $C_L = 0.48$.

An ellipsoidal body with its axis of symmetry and velocity parallel to the streamlines of a simple shear flow can be shown to experience a lift coefficient that is equal to its added mass coefficient (Magnaudet & Eames 2000; Naciri 1992). Using this result together with Moore's theory for the added mass coefficient shows that bubbles with the aspect ratios $\chi = 1.1$ to 1.2 encountered in our study have a slightly increased added mass coefficient $C_L = 0.56$ to 0.62 (Moore 1965; Kushch *et al.* 2002). An alternative estimate can be obtained based on lattice-Boltzmann simulations of deformable bubbles performed by Sankaranarayanan & Sundaresan (2002). These investigators suggested correlating the lift force with the Tadaki number $Ta = ReMo^{0.23}$ where $Mo = g\rho^2\Delta\rho\nu^4/\sigma^3$ is the Morton number and $\Delta\rho$ is the difference between the density of the liquid and gas. The lift coefficient increased with increasing Ta in

simulations for low-*Mo* fluids such as water. However, the simulation for a Tadaki number of about 2 yielded only a modest increase in the lift coefficient to $C_L \approx 0.6$. The Tadaki number in our experiments is smaller still, $Ta \approx 1$, indicating that the effects of deformation on the lift force are modest. At high shear rates or in more viscous fluids, the deformation of the bubble can lead to a decrease or even a change in sign of the lift coefficient. Sankaranarayanan & Sundaresan correlated this behaviour with the capillary number based on the shear rate. Based on the simulations, our experiments fall within the regime for which this decrease would be expected to be small and in any case this effect is in the wrong direction to explain the experimental observations.

It is difficult to establish the effects of bubble volume fraction on the lift coefficient using experimental observations in a disordered bubble suspension, because other effects of bubble–bubble interaction will arise at the same time that the lift force is modified. However, an estimate of the effect of volume fraction on the lift coefficient can be obtained from the numerical simulations of Sankaranarayanan & Sundaresan for bubbles in periodic unit cells. The lift coefficient for nearly spherical high-Reynolds-number bubbles was found to increase only about 10% over a volume fraction range $\alpha = 0$ to 0.08, similar to that considered in our study.

In a study of 500 to 800 μm diameter bubbles in tap water interacting with a vortex ring, Sridhar & Katz (1995) extracted apparent lift coefficients that were much larger than the theoretical estimates mentioned above. These large values may have resulted from effects of surfactants possibly coupled with the highly transient nature of the fluid flow in a reference frame following the bubble motion (Magnaudet & Eames 2000). Since isolated bubbles in our experiments rise with a velocity close to the theoretical estimate for surfactant-free bubbles (Zenit *et al.* 2001) and the bubbles experience a fully developed shear flow, we do not believe that the observations of Sridhar & Katz are relevant to our study.

Thus, it seems unlikely that any possible modification of the lift coefficient to account for deviations from the estimate $C_L = 0.5$ for inviscid flow around a spherical bubble could account for the factor of 2.5 discrepancy between the experiments and a model based on a simple balance of lift forces and buoyancy.

4.2. *Bubble–wall collisions*

Clearly, the sole action of the lift force is not sufficient to explain the moderate velocity gradients found. We conducted additional single-bubble experiments to quantify the effects of bubble–wall collisions. Tsao & Koch (1997) observed that bubbles interacting with a wall with $\theta < 55^\circ$ bounced repeatedly in a periodic motion. If the amplitude of this motion were to grow with decreasing θ to become as large as the channel thickness $W = 2$ cm, then this might account for the distribution of bubbles across the gap. To investigate this possibility, we released bubbles from a single capillary at the base of the inclined channel and observed their motion at a distance of 1 mm above the base using video photography. The mean bouncing amplitude remained of the same order of magnitude as the bubble diameter, so simple bubble–wall interactions do not account for the small bubble volume fraction gradients observed in the experiments.

4.3. *Dispersion of bubbles*

Zenit *et al.* (2001) noted that the variances of the liquid and bubble velocity in a vertical channel bubbly flow are much larger than those expected for a homogeneous bubble suspension. In the present study, we have seen that velocity variances of similar magnitude are retained when the channel is slightly inclined. It is natural to

expect that these fluctuating motions will lead to a dispersion of bubbles that will tend to oppose the development of bubble volume fraction gradients. The frequency spectrum of the liquid velocity fluctuations measured by a hot-film probe that was fixed in space indicated that the dominant frequencies were much smaller than the value u_b/d_b that would be expected in a homogeneous suspension and comparable with u_b/W. The frequency spectrum did not exhibit the ω^{-2} scaling with frequency ω that would be expected for a single-phase turbulent flow. Thus, we believe that the velocity fluctuations are associated with an instability of the bubble suspension that occurs on a length scale of order W rather than being associated with the individual bubble–bubble interactions in a homogeneous suspension or due to liquid-phase turbulence. A better understanding of this phenomenon might be obtained from a full numerical solution of the averaged equations of motion for the three-dimensional time-dependent bubbly flow that occurs in the presence of the clustering instability.

In the absence of this solution, we will make a rough estimate of the dispersive effect of the velocity fluctuations based on the measured bubble velocity variance. The diffusivity of the bubbles can be expressed as the time integral of the two-time autocorrelation for the bubble velocity. Thus, a simple estimate of the diffusivity D is

$$D = \langle u_b'^2 \rangle \tau \tag{4.3}$$

where $\langle u_b'^2 \rangle$ is the bubble velocity variance and τ is the correlation time for the bubble velocity. We postulate that the $O(u_b/W)$ frequency of the liquid velocity observed in the Eulerian liquid velocity power spectrum results from the passage of clusters of bubbles whose size is comparable with the channel thickness W. If bubbles move in and out of these clusters as a result of their fluctuating motion, then we expect

$$\tau = \frac{W}{\langle u_b'^2 \rangle^{1/2}} \tag{4.4}$$

so that

$$D = \langle u_b'^2 \rangle^{1/2} W. \tag{4.5}$$

We measured the variance of the streamwise bubble velocity at various points across the gap thickness of the inclined channels. However, we found that the variance is relatively independent of cross-stream position and independent of the angle of inclination θ, so we will simply take $\langle u_b'^2 \rangle^{1/2}$ from the measurements of the root-mean-square vertical bubble velocity in the vertical channel. To predict the component of the diffusion tensor governing the transport of bubbles across the gap, it would be more appropriate to use the cross-stream velocity variance. However, the impedance probe only provides a measurement of the vertical velocity variance. In very dilute suspensions, we were able to directly visualize the bubble motion and use video image analysis to show that the horizontal velocity variance was smaller than but of the same order of magnitude as the vertical velocity variance. The value of the diffusivity estimated in this way is plotted as a function of volume fraction as the solid line in figure 13. The diffusivity is presented in dimensionless terms, D/ν_f, where ν_f is the kinematic viscosity of water.

We can consider a mass conservation equation for the bubble phase in fully developed steady-state flow that includes the velocities U_{buoy} and U_{lift} due to buoyancy and lift forces and a flux due to the effective diffusivity D of the bubbles

$$\frac{\partial}{\partial y}((U_{\text{buoy}} + U_{\text{lift}})\alpha) - \frac{\partial}{\partial y}\left(D\frac{\partial \alpha}{\partial y}\right) = 0. \tag{4.6}$$

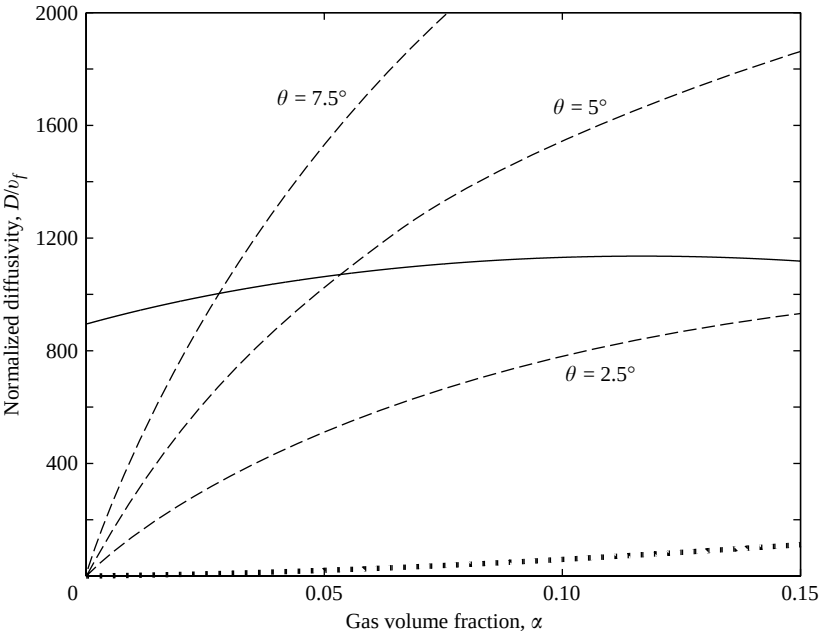

FIGURE 13. Normalized diffusion coefficient as a function of gas volume fraction. The solid line is the hydrodynamic diffusion coefficient estimated on the basis of the measured bubble velocity variance, i.e. equation (4.5). The dashed lines show the diffusivity (4.8) that would be required to balance the buoyancy-driven velocity and explain the measured bubble volume fraction gradient, for different values of the inclination angle, θ. The dotted line shows the diffusivity that is equivalent to the bubble-phase pressure derived from kinetic theory (Kang *et al.* 1997).

where $U_{\text{buoy}} = u_b \sin(\theta)$ is the component of the bubble's buoyancy-driven velocity in the direction perpendicular to the walls. The lift velocity can be obtained by balancing the lift force with a viscous drag force, yielding

$$U_{\text{lift}} = -\frac{d_b^2 C_L v_b \partial u_b/\partial y}{36\mu} \tag{4.7}$$

where we have approximated the liquid velocity gradient by the bubble velocity gradient, which in turn can be obtained from the measurements given in figure 8.

Before comparing solutions of (4.6) with the measured bubble volume fraction gradient, let us consider whether the order of magnitude of the effective diffusivity predicted on the basis of the bubble velocity fluctuations (solid line in figure 13) is comparable with the diffusivity that would be needed to prevent the accumulation of bubbles at the top of the channel gap. Equation (4.6) would be satisfied exactly if

$$D = \frac{(U_{\text{buoy}} - U_{\text{lift}})\alpha}{\partial\alpha/\partial y}. \tag{4.8}$$

This value of D needed to balance the buoyancy and lift fluxes is plotted as the dashed lines in figure 13 (considering different values of the channel inclination angle, θ). Thus, we see that the estimate of the bubble effective diffusivity is comparable in magnitude with the value needed to explain the small bubble volume fraction gradients reported in § 3.3. This corroborates the importance of hydrodynamic diffusion in maintaining relatively modest bubble volume fraction gradients even in the presence of a significant

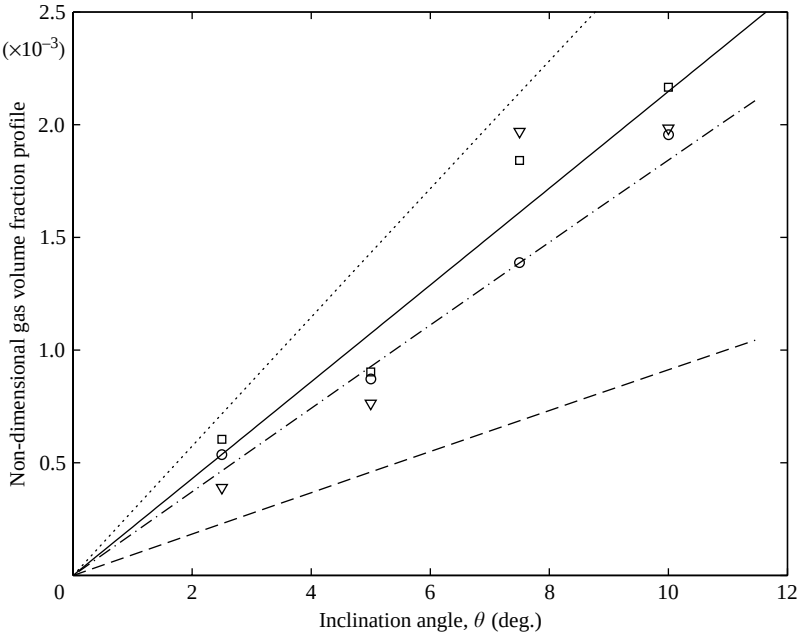

FIGURE 14. Comparison of the measured non-dimensional gas volume fraction gradient with predictions from (4.6). The predictions are for three mean gas volume fractions: — — —, $\alpha = 0.02$; — · —, $\alpha = 0.05$; · · ·, $\alpha = 0.10$. The circles, squares and triangles refer to experiments with $\alpha = 0.02$, 0.05, and 0.10, respectively. The solid line shows a best fit to all of the experimental results, which exhibit little dependence on volume fraction.

segregating buoyancy driving force. There is a significant difference in the volume fraction dependence of the two estimates of the diffusivity but this could easily result from the rough approximation made in estimating the correlation time for bubble velocities.

Alternatively, we can compare the predictions of (4.6) using the estimated diffusivity (equation (4.5)) with the measured gradients in the bubble volume fraction. This comparison is shown in figure 14. The predicted and measured volume fraction gradients are of similar magnitude and both grow linearly with the angle of inclination. However, the predictions overestimate the dependence of the volume fraction gradient on the value of the mean volume fraction.

The values of D estimated by (4.8) and (4.5) are much larger than the dispersion that is predicted by the kinetic theory for a homogeneous sheared suspension (Kang *et al.* 1997). To compare the bubble-phase pressure P predicted by Kang *et al.* with a diffusivity, we note that balancing the pressure gradient with the drag force acting on the bubbles yields a velocity

$$u_{bp} = -\frac{\nabla P}{6\pi\mu n d_b R_d} \tag{4.9}$$

where $n = 6\alpha/(\pi d_b^3)$ is the number of bubbles per unit volume and $R_d(\alpha)$ is the ratio of the average drag in the suspension to the drag on a single bubble. Equating the flux $u_{bp}\alpha$ to the diffusion flux $-D\nabla\alpha$, we can express a diffusivity that is equivalent

to the bubble-phase pressure as

$$D = \frac{1}{36\mu d_b R_d}\frac{\partial P}{\partial \alpha}. \tag{4.10}$$

Batchelor (1988) and Nott & Brady (1994) have discussed the relationship between the concepts of hydrodynamic diffusion and dispersed-phase pressure. Using (4.10), the measured bubble-phase temperature and the kinetic theory result for the bubble-phase pressure yields a diffusivity (plotted as the dotted line in figure 13) that is 10 times smaller than that required to explain the measured volume fraction gradient. The kinetic theory assumes that the fluctuations in the velocities of individual bubbles are nearly uncorrelated with the fluid velocity fluctuations. This assumption is valid when the viscous relaxation time of the bubbles $\tau_v = \rho_f d_b^2/(72\mu)$ is much smaller than the time scale over which the fluid velocity fluctuates. This assumption holds for a homogeneous, high-Reynolds-number bubble suspension. However, the clustering in the bubbly channel flow leads to liquid velocity fluctuations that remain correlated over $O(W/\langle u_b'^2\rangle)$ times which are a factor of 10–15 larger than τ_v.

4.4. *Effective viscosity and slip coefficient*

In the previous subsection, we discussed the various mechanisms controlling the bubble's cross-stream motion perpendicular to the channel walls and saw that a combination of hydrodynamic dispersion and a lift-force-driven velocity balance the buoyancy-driven motion of the bubbles and maintain a modest bubble volume fraction gradient. In this subsection, we will examine the streamwise bubble motion driven by this bubble volume fraction gradient.

Consider a streamwise momentum balance for the suspension mixture (bubbles and liquid). In a vertical channel, the volume fraction is independent of cross-stream position y and the buoyancy force can be balanced by a change in the axial liquid pressure gradient in such a way that there is no variation of the mixture velocity with y. In the inclined channel, the variation of the bubble volume fraction results in a variable buoyancy force across the channel thickness that is expected to drive a shearing motion in the liquid. Since the average flow is fully developed, the inertial terms associated with the mean velocity are zero. However, a Reynolds stress term arises from the velocity fluctuations in the liquid driven by the random motion of individual bubbles and bubble clusters. We will model this Reynolds stress in terms of an effective viscosity μ_{eff} times the gradient of the mean liquid velocity, so that the streamwise mixture momentum equation is

$$\frac{\partial}{\partial y}\left(\mu_{\text{eff}}\frac{\partial u_{lv}}{\partial y}\right) = -\rho g\cos\theta\left(\alpha_0 + y\frac{\partial \alpha}{\partial y}\right) + \frac{\partial p_f}{\partial z}. \tag{4.11}$$

In a fully developed flow, the pressure gradient in the fluid $\partial p_f/\partial z$ is independent of y and its value can be chosen such that the integral of the liquid velocity across the gap thickness is zero. Because the effective viscosity in (4.11) arises from the inertia associated with the liquid velocity fluctuations it is expected to be $O(Re)$ larger than the fluid viscosity. Kang *et al.* (1997) predicted that a large effective viscosity would arise from the Reynolds stress terms in a homogeneous, sheared bubbly liquid in the absence of a buoyancy-driven relative motion of the two phases. We have noted that the buoyancy-driven relative motion of the two phases leads to clustering of bubbles and a liquid velocity variance that is much larger than that predicted for a homogeneous bubble suspension. The effective viscosity arising in our experiments may thus be expected to be even larger than that predicted by Kang *et al.*

Note that for the above balance equation, the z-component of the lift force has been neglected. Since, as discussed in § 4.1, there is a local relative velocity (between the bubble and the fluid) in the y-direction and the vorticity of the fluid is in the x-direction, a lift force would act on the z-direction. However, the resulting lift z-velocity can be shown to be small compared with the buoyancy-driven z-velocity; therefore, it can be neglected.

A momentum balance for the liquid phase alone is dominated by a balance between the interphase drag between the bubbles and liquid and a pressure gradient in the liquid phase. The viscosity of the liquid can be neglected throughout most of the channel thickness. This balance leads to a nearly constant relative velocity of the bubble and liquid since the bubble volume fraction and therefore the drag coefficient are nearly independent of y. As a result, the variations of the liquid, bubble and mixture velocities with respect to y are nearly equal and any one of the velocities could have been used in the viscous stress term in (4.11). This observation was used in § 4.1 to determine the liquid velocity gradient and the lift forces acting on the bubble from the measured bubble velocity gradient.

The force balance that prevails throughout the bulk of the suspension can lead to a non-zero mean liquid velocity near the wall. Bubble–wall collisions are not sufficient to lead to a zero velocity of the bubbles adjacent to the wall, so the bubbles exert a non-zero force on the liquid at $O(a)$ distances from the wall. Owing to the small liquid viscosity, the mean liquid velocity can vary rapidly in a boundary layer less than one bubble radius from the wall where the drag exerted by the bubbles is reduced because of the excluded volume of the wall. For simplicity, we will model the effect of this boundary layer as giving rise to a simple Maxwell slip boundary condition applied to the outer approximation for the liquid velocity as one approaches the boundary layers at the channel walls:

$$u_{lv} = \mp\lambda \frac{\partial u_{lv}}{\partial y} \quad \text{at} \quad y = \pm\frac{W}{2}. \tag{4.12}$$

Here λ is the Maxwell slip length which will be determined from the experimental measurements for the wall shear stress. Note that the bubble, liquid and mixture velocities will all be non-zero near the wall in the sheared suspension. We might have chosen to apply a slip boundary condition to the bubble or mixture velocity. However, only the choice of the liquid velocity in (4.12) results in a constant bubble velocity and zero mean liquid velocity in a vertical channel for all values of y.

Integrating (4.11) assuming that the effective viscosity and bubble volume fraction gradients are independent of y and applying the boundary conditions (4.12) yields the liquid velocity profile:

$$u_{lv} = \frac{\rho g}{6\mu_{\text{eff}}} \frac{\partial \alpha}{\partial y} \cos\theta \left[y \left(\frac{W}{2} \right)^2 \frac{1 + 3\lambda^*}{1 + \lambda^*} - y^3 \right] \tag{4.13}$$

where $\lambda^* = 2\lambda / W$.

The shear stress at the wall is

$$\tau|_{wall} = -\mu_{\text{eff}} \left. \frac{\partial u_{lv}}{\partial y} \right|_{y=H/2} = \frac{\rho g}{3} \cos(\theta) \frac{\partial \alpha}{\partial y} \left(\frac{W}{2} \right)^2 \frac{1}{1 + \lambda^*}. \tag{4.14}$$

The value of the slip coefficient can be obtained by comparing (4.14) with the shear stress measured by the flush-mounted hot-film probe. The value of λ^* that gives the best fit to all the data for the values of α and θ where large instabilities are not

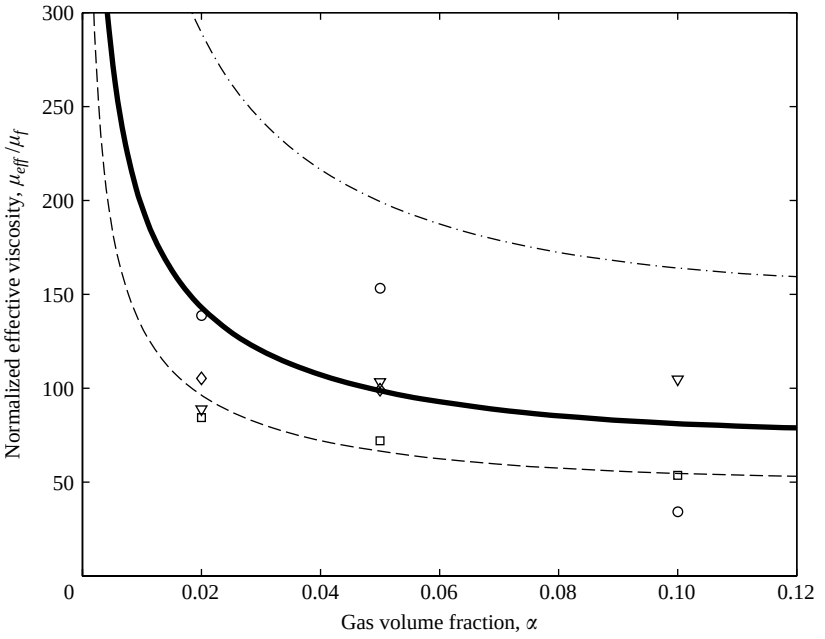

FIGURE 15. Suspension effective viscosity calculated from (4.15) for four channel inclinations as a function of the gas volume fractions: ○, $\theta = 2.5°$; □, $\theta = 5°$; ▽, $\theta = 7.5°$; ◇, $\theta = 10°$. The lines show the predictions from (4.15) for different values of λ^*: ——, $\lambda^* = 0.32$; – – –, $\lambda^* = 0$ (no slip condition); –·–, $\lambda^* = \infty$ (no tangential stress condition). To obtain the lines equations (3.3) and (3.5) were used.

observed is $\lambda^* = 0.32$. In figure 12, the predictions based on (4.14) are plotted as solid lines and compared with the experimental measurements.

The value of the effective viscosity can be found using the value of λ^* obtained from the wall shear stress measurements along with the measured volume fraction and bubble velocity profiles. We were only able to accurately measure the bubble velocity in the central portion of the channel and so we use the value of the velocity gradient at the centre of the channel for this analysis. Assuming that the bubble and liquid velocity gradients are equal, the effective viscosity can be obtained from (4.13) and is given by

$$\mu_{\text{eff}} = \frac{\rho g \cos(\theta)}{6(\partial u_b/\partial y)\big|_{y=0}} \frac{\partial \alpha}{\partial y} \left(\frac{W}{2}\right)^2 \frac{1+3\lambda^*}{1+\lambda^*}. \tag{4.15}$$

Figure 15 shows the suspension effective viscosity calculated using the results from figure 8 for the bubble velocity gradient and figure 6 for the bubble concentration gradient. The viscosity is normalized by the viscosity of the liquid phase, $\mu_f = 0.001$ Pa s. The data points are calculated considering a value of $\lambda^* = 0.32$. Note that the viscosity of the suspension is on the order of 100 times greater than the viscosity of water. The apparent viscosity does not show a clear variation with respect to the inclination of the channel or the gas volume fraction. To give some indication of the uncertainty in the effective viscosity associated with the value of the slip coefficient, we also show results based on an assumption of no slip ($\lambda^* = 0$) and no tangential stress ($\lambda^* = \infty$) boundary conditions.

The shear viscosity of a stable homogeneous suspension of bubbles with potential-flow liquid velocity disturbances can be derived from kinetic theory arguments (Spelt & Sangani 1998):

$$\mu_{KT} = \frac{16}{5\pi^{1/2}} C_k \rho_f d_b T^{1/2} \alpha^2 g_c \left(1 + \frac{\pi}{2}\left(1 + \frac{5}{8\alpha g_c}\right)^2\right) \tag{4.16}$$

where C_k is the added mass coefficient associated with the fluctuating motion of the bubbles, g_c is the pair probability of the bubbles for bubble–bubble contact, and T is the bubble-phase temperature. If we calculate the bubble-phase temperature from the measured bubble velocity variance, as in § 3.5, an estimation for μ_{KT} can be found. This predicted effective viscosity for a homogeneous suspension is only about 3 to 5 times larger than the fluid viscosity and is much smaller than the effective viscosities measured in the experiments. This is not surprising since we have already noted that bubble clustering contributes strongly to the bubble velocity variance and the effective diffusivity of the bubbles. A critical assumption in the kinetic theory is that the liquid velocity fluctuations that give rise to momentum transport are only correlated over the $O(a/\langle u_b' \rangle)$ time between successive collisions of one bubble with other bubbles in the suspension. The liquid velocity spectrum measured in Zenit *et al.* (2001) indicated much longer correlation times for the liquid velocity. Since the effective kinematic viscosity, given by the product of the bubble velocity variance and the correlation time of the bubble velocity fluctuations, has a very large correlation time it is expected to be of $O(Re(W/d_b))$.

The use of an effective viscosity to describe the average momentum transport in an unstable, clustered bubble suspension is not likely to be quantitatively accurate. A more complete description would require three-dimensional numerical simulations of the fluid and bubble velocity fluctuations that arise in the unstable suspension. However, like an eddy viscosity model of a turbulent flow, this description provides a simple framework in which to interpret the experimental results. The large effective viscosity leads to velocity gradients that are on the order of 100 times smaller than one would predict in a single-phase (water) flow with the same buoyancy driving force.

4.5. *Bubble clustering*

It is well known that bubbles rising in an inviscid liquid and under the potential-flow approximation tend to cluster in horizontal rafts. This instability arises naturally due to the nature of the hydrodynamic interaction between individual bubbles. Although this effect has been calculated numerically (for a modest number of bubbles), our experimental measurements have shown that clustering is not as strong as that observed in the numerical calculations (Zenit *et al.* 2001). In the numerical simulations of Sangani & Didwania (1993*b*), all of the bubbles form coherent horizontal rafts that span the periodic cell. However, in the experiments, the clustering could only be detected by a careful statistical analysis of video images and was more apparent through its indirect effect of producing large-amplitude, slowing varying liquid velocity fluctuations.

In the theory of Spelt & Sangani (1998), the clustering instability arises from a negative pressure due to the hydrodynamic interactions among a suspension of bubbles moving with a common velocity. This pressure which is analogous to a

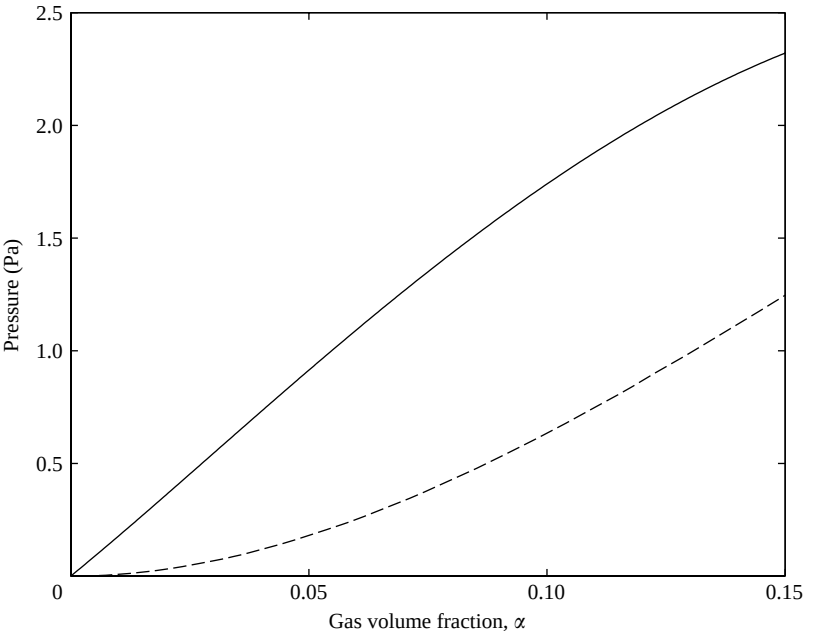

FIGURE 16. Bubble-phase pressure obtained using (4.19) (solid line) and the negative of the Maxwell pressure (dashed line), (4.17), as functions of gas volume fraction.

Maxwell pressure in electrostatics was determined by Spelt & Sangani (1998) to be

$$P_{\text{Maxwell}} = -\frac{1}{2}\,\rho_f \alpha^2 \left(\frac{C_a}{2} + 1\right)^2 v_b^2 \tag{4.17}$$

where C_a is the added mass coefficient which is a function of the gas volume fraction. According to Spelt & Sangani, C_a is of the form

$$C_a = \frac{1 + 2\alpha}{1 + \alpha}. \tag{4.18}$$

Using (4.10), we can express the diffusivity due to the bubble velocity fluctuations (4.5) in terms of a pressure:

$$P = \frac{36\mu\alpha D}{d_b^2}. \tag{4.19}$$

This estimate assumes that D is independent of the gas volume fraction and neglects dissipation effects. This positive pressure contribution is compared with the negative of the Maxwell pressure in figure 16. Although the estimates of P include some experimental uncertainty, it is clear that the two pressures are of the same order of magnitude. This comparison may explain why the experimentally determined clusters are not as strong as those predicted by the theory. The bubble clusters may grow until they produce a sufficiently large velocity disturbance and bubble diffusion to stabilize the suspension against the further growth of clusters.

4.6. *Instability*

It has been observed by many researchers (Lin *et al.* 1996; Lammers & Biesheuvel 1996 for example) that large vortical structures appear in bubble columns. Such structures that move up and down and extend across the entire channel were observed

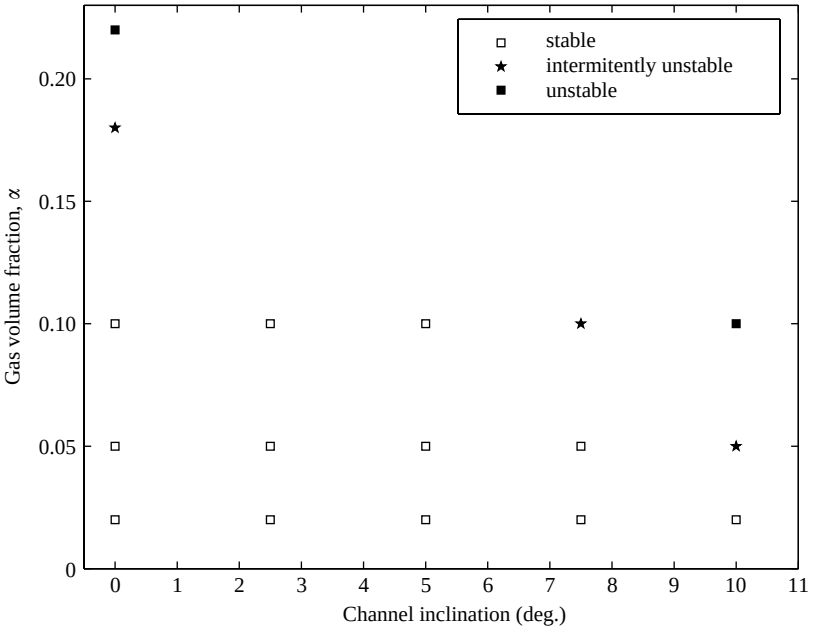

FIGURE 17. Map of the stability conditions of bubble suspensions.

in our experiments on vertical channel flow (Zenit *et al.* 2001) for concentrations larger than 0.20. The occurrence of such large-scale instabilities is generally postulated to be associated with concentration waves.

In the case of the inclined channel, evidence of the instability was observed at lower concentrations and depended on the channel inclination angle. Figure 17 shows a map of the conditions at which the instability was first observed. The onset of instability was determined visually and it was further corroborated by the nature of the fluid velocity spectrum. A noticeable peak at the low-frequency range could be identified when the unsteady vortical motion appeared. The instability appears at large bubble concentrations when the channel inclination is small. As the channel inclination increases the instability is observed at lower concentrations. The strength of the shear clearly affects the onset of the instability.

A criterion to establish the onset of instability can be obtained from the gradient of the dispersed-phase pressure with respect to concentration. This criterion is discussed by Batchelor (1988) who argues that a homogeneous suspension cannot be stable if the derivative of the dispersed-phase pressure with respect to the concentration is negative. In general this derivative must be larger than some critical value to overcome destabilizing influences such as that due to volume-fraction-dependent drag and inertia.

Figure 18 shows the gradient of the total bubble-phase pressure with respect to the bubble concentration. The gradient is calculated as

$$\frac{\partial P_t}{\partial \alpha} = \frac{\partial}{\partial \alpha}(P + P_{\text{Maxwell}}). \tag{4.20}$$

The pressure gradient obtained from the diffusion coefficient calculated from the bubble velocity variance, depicted by the solid line, (equation (4.5)) predicts that the instability will appear at concentrations higher than 0.11. On the other hand, the pressure gradient predicted from the diffusivity coefficient inferred from the

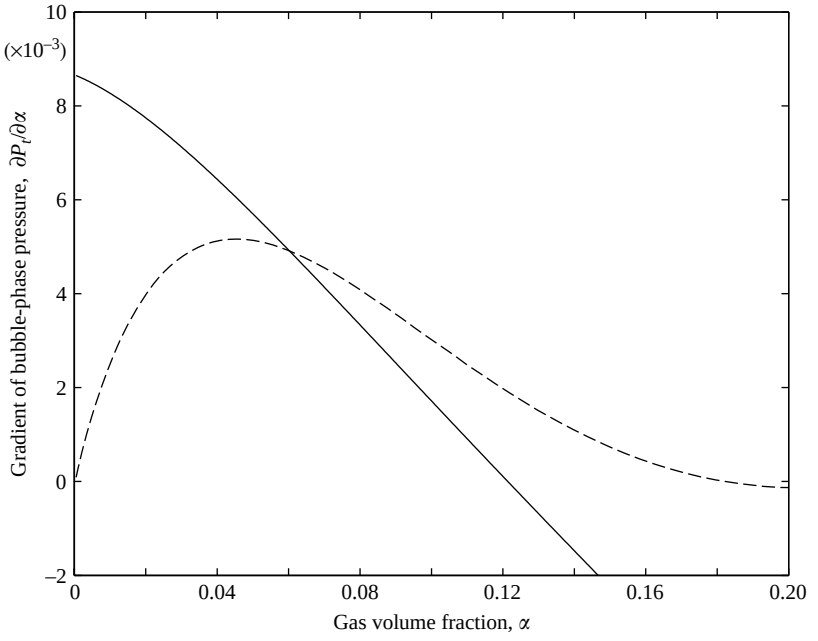

FIGURE 18. Gradient of the total bubble-phase pressure with respect of the bubble concentration as a function of the gas volume fraction. The solid and dashed lines show the prediction of the pressure gradient based on (4.5) and (4.8) respectively.

concentration gradient, depicted by the dashed line, (equation (4.8)) shows a stable state up to concentrations of 0.183. The estimates of the onset of instability are in rough agreement with that observed experimentally in the vertical channel.

5. Conclusions

We have examined the behaviour of a monodisperse suspension of high-Reynolds-number, low-Weber-number bubbles in a narrow channel that is slightly inclined to gravity (angles of inclination less than 10°). This novel flow configuration enables one to examine the small perturbations of the suspension resulting from a weak segregating force (the component of the buoyancy force acting across the channel) and a weak shearing motion driven by buoyancy variations across the gap. The measured volume fraction and bubble velocity profiles across the gap were interpreted as providing evidence of the transport of bubbles and momentum due to bubble-induced fluid velocity fluctuations. The narrow gap allowed the suspension to attain a fully developed unidirectional flow with no visually apparent instability for a range of gap-averaged bubble volume fractions and inclination angles. It might be interesting in the future to use this configuration to investigate the behaviour of a range of inertial suspensions, such as fluidized beds or bubble suspensions in fluids with higher viscosity and/or lower interfacial tension.

Inclined channels are commonly used to enhance the rate of gravitational separation of particles and fluid in suspension where the particle Reynolds number is very small

(Kapoor & Acrivos 1995). In that situation, a distinct interface forms at some position across the gap between the suspension and a clear fluid layer. In the high-Reynolds-number suspension studied here, the hydrodynamic diffusion of the bubbles is found to be large enough that no clear fluid layer forms and, in fact, the variation of bubble volume fraction across the gap is quite modest.

The transport of bubbles and momentum was much more efficient than that predicted by theories for homogeneous bubbly liquids (Kang *et al.* 1997; Spelt & Sangani 1998). However, these theories predict that the homogeneous state of a suspension of bubbles rising due to buoyancy is unstable to the formation of bubble clusters. Although these clusters are not readily apparent to the naked eye, Zenit *et al.* (2001) showed that video photography demonstrated an enhanced probability of horizontal bubble pairs. Also, the liquid velocity variance and the frequency spectrum of the liquid velocity gave evidence of large-scale liquid motions that we believe are induced by bubble clusters. Since the current experiment represents a weak perturbation to the state of bubbles rising in a vertical column, the shearing motion in the inclined channels is not expected to be sufficient to break up the clusters or provide a sufficient source of bubble-phase pressure to stabilize the suspension. The large values of the effective viscosity and bubble-phase diffusivity (or bubble-phase pressure) deduced from the present experiments are consistent with the presence of large-scale bubble clusters. The extent of bubble clustering in the experiment was considerably less than that seen in numerical simulations of $O(50)$ bubbles undergoing potential-flow interactions. We found that the bubble-phase pressure induced by the hydrodynamic fluctuations was comparable to the negative Maxwell pressure that is predicted to induce clustering. This suggests the idea that the bubble clustering may proceed to such an extent that the clusters produce enough bubble-phase pressure to prevent further clustering.

A more vigorous and visually obvious instability occurred for bubble volume fractions larger than 0.2 in the vertical channel and at lower volume fractions with increasing angles of inclination. The instability in the vertical channel may be similar to that observed in previous studies (Lin *et al.* 1996; Lammers & Biesheuvel 1996 for example) and attributed to the growth of void-fraction waves associated with the volume-fraction dependence of the bubble drag coefficient. We found that this instability sets in at approximately the volume fraction above which the bubble-phase pressure (obtained as the sum of the Maxwell and hydrodynamic-fluctuation contributions) fails to increase with increasing volume fraction, so that it no longer stabilizes the homogeneous state. It would be interesting to obtain a better understanding of how the shear induced by inclining the channel influences the instability of the suspension. The instability of sheared granular materials has been studied extensively (for example, Wang, Jackson & Sundaresan 1996) but we are not aware of comparable studies of sheared inertial suspensions in which the continuous phase plays an important role.

The experiments presented here suggest that the transport of bubbles and momentum resulting from the fluctuating motion in a suspension can play an important role in limiting the extent of segregation of the disperse phase and producing significant stresses with modest gradients of mean velocity. It is important to develop a better understanding of the origin of this fluctuating motion. Kinetic theories of sheared granular materials (Lun *et al.* 1984), gas–solid suspensions (Sangani *et al.* 1996), and bubble suspensions (Kang *et al.* 1997) consider the fluctuating motions induced by individual particles or bubbles as they collide with one another. Other studies have considered how an assumed turbulent flow in the continuous phase may

be modified by the presence of particles (Ahmed & Elghobashi 2000). However, in the present situation, the fluctuating motion is believed to result primarily from the instabilities arising from the inherent dispersed nature of the flow. Little is known at present about the magnitude of this type of fluctuating motion. Since most inertially dominated suspensions are subject to some form of instability, the resulting fluctuating motions can be expected to influence a broad range of multiphase flows.

This work was supported by NASA under grant number NAG3-1853 and by CONACyT grant number J34497U-2.

REFERENCES

Ahmed, A. M. & Elghobashi, S. 2000 On the mechanisms of modifying the structure of turbulent homogeneous shear flows by dispersed particles. *Phys. Fluids* **12**, 2906–2930.

Auton, T. R. 1987 The lift force on a spherical body in a rotational flow. *J. Fluid Mech.* **183**, 199–218.

Batchelor, G. K. 1988 A new theory of the instability of a uniform fluidized bed. *J. Fluid Mech.* **193**, 75–110.

Biesheuvel, A. & Gorissen W. C. M. 1990 Void fraction disturbances in a uniform bubbly fluid. *Intl J. Multiphase Flow* **16**, 211–231.

Bulthuis, H. F., Prosperetti, A. & Sangani, A. S. 1995, Particle stress in disperse two-phase potential flow. *J. Fluid Mech.* **294**, 1–16.

Couderc, J. P. 1985 Incipient fludization and particulate systems. In *Fluidization* (ed. J. Davidson, R. Clift & D. Harrison), 2nd Edn. Academic.

Duineveld, P. C. 1995 The rise and shape of bubbles in pure water at high Reynolds number. *J. Fluid Mech.* **292**, 325–332.

Jensen, B. L., Sumer, B. M. & Fredsoe, J. 1989 Turbulent oscillatory boundary layers at high Reynods numbers. *J. Fluid Mech.* **206**, 206–265.

Kang, S. A., Sangani, A. S., Tsao, H.-K. & Koch, D. L. 1997 Rhelogy of dense bubble suspensions. *Phys. Fluids* **9**, 1540–1570.

Kapoor, B. & Acrivos, A. 1995 Sedimentation and sediment flow in settling tanks with inclined walls. *J. Fluid Mech.* **290**, 39–66.

Kushch, V. I., Sangani, A. S., Spelt, P. D. M. & Koch, D. L. 2002 Finite-Weber-number motion of bubbles through a nearly inviscid liquid. *J. Fluid Mech.* **460**, 241–280.

Lammers, J. H. & Biesheuvel, A. 1996 Concentration waves and the instability of bubbly flows. *J. Fluid Mech.* **328**, 67–93.

Lance, M. & Bataille, J. 1991 Turbulence in the liquid phase of a uniform bubbly air-water flow. *J. Fluid Mech.* **222**, 95–118.

Leighton, D. T. & Acrivos, A. 1987 Measurements of shear-induced difusion in concentrated suspensions of spheres. *J. Fluid Mech.* **177**, 109–131.

Lin, T.-J., Reese, J., Hong, T. & Fan, L.-S. 1996 Quantitative analysis and computations of two dimensional bubble columns. *AIChE J.* **42**, 301–318.

Liu, T. J. & Bankoff, S. G. 1993*a* Structure of air-water bubbly flow in a vertical pipe–I. Liquid mean velocity and turbulence measurments. *Intl J. Heat Mass Transfer* **36**, 1049–1060.

Liu, T. J. & Bankoff, S. G. 1993*b* Structure of air-water bubbly flow in a vertical pipe–II. oid fraction, bubble velocity and bubble size distribution. *Intl J. Heat Mass Transfer* **36**, 1061–1072.

Lu, G. Z., Bittorf, K., Thompson, B. G. & Gray, M. R. 1997 Liquid circulation and mixing in an inclined bubble column. *Can. J. Chem. Engng* **75**, 290–298.

Lun, C. K. K., Savage, S. B., Jeffrey, D. J. & Chepurniy, N. 1984 Kinetic theories for granular flow – inelastic particles in Couette-flow and slightly inelastic particles in a general flowfield. *J. Fluid Mech.* **140**, 223–256.

Magnaudet, J. & Eames, I. 2000 The motion of high-Reynolds-number bubbles in inhomogeneous flow. *Annu. Rev. Fluid Mech.* **32**, 659–708.

Magnaudet, J. & Legendre, D. 1998 Some aspects of the lift force on a spherical bubble. *Appl. Sci. Res.* **58**, 441–461.

Moore, D. W. 1965 The velocity of rise of distorted gas bubbles in a liquid of small viscosity. *J. Fluid Mech.* **23**, 749–749.

Naciri, A. 1992 Contribution a l'etude des forces exercees par un liquide sur une bulle de gaz: portance, masse ajoutee et interactions hydrodynamiques. PhD thesis, Ecole Centrale de Lyon, Ecully, France.

Nott, P. R. & Brady, J. F. 1994 Pressure-driven flow of suspensions: simulations and theory. *J. Fluid Mech.* **275**, 157–199.

Parthasarathy, R. N. & Faeth, G. M. 1990 Turbulence modulation in homogeneous dilute particle-laden flows. *J. Fluid Mech.* **220**, 485–514.

Sangani. A. S. & Didwania, A. K. 1993*a* Disparse phase stress tensor in flows of bubbly liquids at large Reynolds numbers. *J. Fluid Mech.* **248**, 27–54.

Sangani, A. S. & Didwania, A. K. 1993*b* Dynamics simulations of flows of bubbly liquids at large Reynolds numbers. *J. Fluid Mech.* **250**, 307–337.

Sangani, A. S., Mo, G. B., Tsao, H. K. & Koch, D. L. 1996 Simple shear flows of dense gas-solid suspensions at finite Stokes numbers. *J. Fluid Mech.* **313**, 309–341.

Sankaranayanan, K. & Sundaresan, S. 2002 Lift force in bubbly suspensions. *Chem. Engng Sci.* **57**, 3521–3542.

Smereka, P. 1993 On the motion of bubbles in a periodic box. *J. Fluid Mech.* **254**, 79–112.

Spelt, P. D. M. & Sangani, A. S. 1998 Properties and averaged equations for flows of bubbly liquids. *App. Sci. Res.* **58**, 337–386.

Sridhar, G. & Katz, J. 1995 Drag and lift forces on microscopic bubbles entrained by a vortex. *Phys. Fluids* **7**, 389–399.

Tsao, H.-K. & Koch, D. L. 1997 Observations of high Reynolds number bubbles interacting wityh a rigid wall. *Phys. Fluids* **9**, 2591–2600.

Valukina N. V., Koz'menko, B. K. & Kashinskii 1979 Characteristics of a flow of monodisperse gas-liquid mixture in a vertical tube. *Inzhenerno-Fizicheskii Zhurnal* **36**, 695–698.

Wang, C. H., Jackson, R. & Sundaresan, S. 1996 Stability of bounded rapid shear flows of a granular material *J. Fluid Mech.* **308**, 31–62.

Wang, S. K., Lee, S. J., Jones, O. C. & Lahey, R. T. 1987 3-D turbulence structure and phase distribution measurements in bubbly two-phase flows. *Intl J. Multiphase Flow* **8**, 327–343.

Yurkovetsky, Y. & Brady, J. F. 1994 Statistical mechanics of bubbly liquids. *Phys. Fluids* **8**, 881–895.

Zenit, R., Koch, D. L. & Sangani, A. S. 2001 Measurements of the average properties of a suspension of bubbles rising in a vertical channel. *J. Fluid Mech.* **429**, 307–342.

Zenit, R., Koch, D. L. & Sangani, A. S. 2003 Impedance probe to measure local gas volume fraction and bubble velocity in a bubbly liquid. *Rev. Sci. Intstrum.* **74**, 2817–2827.

Zhang, D. Z. & Prosperetti, A. 1994 Averaged equations for inviscid disperse two-phase flow. *J. Fluid Mech.* **267**, 185–219.